Structural and impedance spectroscopic study of Zn-substituted Ba5CaTi2Nb8O30 tetragonal tungsten bronze ceramics

Amine Bendahhou, Pascal Marchet, Soufian El Barkany, Mohamed Abou-Salama

Structural and impedance spectroscopic study of Zn-substituted Ba$_5$CaTi$_2$Nb$_8$O$_{30}$ tetragonal tungsten bronze ceramics

Amine Bendahhou[a*], Pascal Marchet[b], Soufian El Barkany[a], Mohamed Abou-salama[a]

[a]Laboratory of Molecular Chemistry, Materials and Environment, Department of Chemistry, Faculty Multidisciplinary Nador, University Mohamed Premier, B.P. 300, Selouane, Nador 62700, Morocco

[b]IRCER – UMR CNRS 7315, Centre Européen de la Céramique, 12 Rue Atlantis, F-87068 Limoges Cedex, France

* corresponding author:

Email address: bendahhou_amine1718@ump.ac.ma (A. Bendahhou)

Abstract

Zn-doped tungsten bronze compounds derived from Ba$_5$CaTi$_2$Nb$_8$O$_{30}$, with Ba$_5$CaTi$_{2-x}$Zn$_x$Nb$_8$O$_{30}$ composition (x=0; 0.04 and 0.08) were synthesized by the conventional solid-state reaction route. Both solubility of Zn in Ba$_5$CaTi$_2$Nb$_8$O$_{30}$ and tungsten bronze formation with the P4bm space group were verified by the Rietveld method using X-ray diffraction data. The average crystallite size was of the order of 0.08 μm according to Scherrer's formula. SEM micrographs of Ba$_5$CaTi$_{2-x}$Zn$_x$Nb$_8$O$_{30}$ ceramics showed high densification, low porosity, thus a homogeneous grain distribution of different sizes over the entire surface. The average grain size was in the range of 1.3 to 1.6 μm. The frequency-dependent electrical properties were analyzed by complex impedance spectroscopy. Different types of studies such as the Nyquist plot, real and imaginary impedance, conductivity, modulus formalism, and charge carrier activation energy were used to explain the microstructure-electrical properties relationships.

Keywords: Tetragonal tungsten bronze; Ceramics; Oxygen vacancies (OVs); Impedance spectroscopy; AC conductivity; Modulus spectrum

1. Introduction

Lead-free materials have an important place in electronics due to technological progress, the toxicity of lead and the need to protect the environment [1-3]. In order to develop the application of lead-free ceramics, intensive research has been realized in the improvement of the electrical properties of various ferroelectric materials [4-10]. Recently, tungsten-bronze compounds have been considered as one of the candidates to replace lead-based compounds [11, 12]. As for perovskites, tungsten-bronze compounds (TTBs) have also attracted attention

recently for their remarkable dielectric and ferroelectric properties and their various applications in the electronic, chemical and energy conversion sectors [13-16]. TTBs consist of distorted BO_6 octahedra linked by their summits, leading to three different kinds of sites between them: A1, A2, and C. Thus, their general formula is $[(A1)_2(A2)_4(C)_4][(B1)_2(B2)_8]O_{30}$. The pentagonal A2 and square A1 sites can receive large cations such as Ba^{2+}, Ca^{2+}, Sm^{3+} while the triangular sites C receive small cations such as Li^+ [17-19]. The octahedral sites B1 and B2 are occupied by highly charged cations, such as V^{5+}, Ta^{5+}, Zn^{2+} [20-22]. In our study, the smallest site C is unoccupied and thus their general formula becomes $[(A1)_2(A2)_4][(B1)_2(B2)_8]O_{30}$. The variety of cationic sites (A1, A2, C, B1, and B2) gives rise to a great variety of structures, allowing the modulation of the characteristics of TTBs, by substitutions in A1 and A2 sites or in B1 and B2 octahedrons.

Furthermore, complex impedance spectroscopy (CIS) is a powerful non-destructive technique for analyzing temperature and frequency dependent electrical and microstructural properties [23]. CIS allows the evaluation of the relaxation frequency / relaxation time of charge carriers in the material, which is a characteristic property of the samples. CIS also allows the study of conductivity as a function of frequency, modulus spectra, relative permittivity and dielectric losses. The study of impedance data (real part and imaginary part) allows to distinguish between the bulk contribution (grains) and the grain boundaries effects [24, 25].

As mentioned above, much attention has been given recently to compounds with a TTB structure and the modulation of their properties by substitutions. The extensive study of the literature reveals that most work has been realized on rare earth substituted compounds such as $Ba_5RTi_3Nb_7O_{30}$, $Ba_4R_2Ti_4Nb_6O_{30}$ (R = Nd, Sm, Eu, Gd, Dy...) [26-29]. No results were found on the incorporation of Zn^{2+} in $Ba_5CaTi_2Nb_8O_{30}$. In our case, the Ti^{4+} ion, which is tetravalent, is substituted by Zn^{2+} which is bivalent. Thus, this heterogeneous substitution leads to a change in the charge of the "B1, and B2" sites, compensated by the creation of oxygen vacancies (OVs). Oxygen vacancies are one of the most important modifying factors that cannot be ignored for all oxide materials. Oxygen vacancies can be created by heterogenous doping [30], by the use of reducing atmosphere [31, 32] or valence equilibrium [33, 34]. However, few studies have been published on the influence of oxygen vacancies on the structure and dielectric properties of TTB ceramics.

Recently a lot of research has been focused on improvement of the electrical properties of TTBs by substitutions, study of impedance data to distinguish between the bulk contribution (grains) and the grain boundaries effects, identify of the elements which are responsible for the

2

conduction phenomenon in TTB ceramics at high temperature. The researchers have observed that change in Na^+ content has a significant effect on the electrical properties of $(Sr_{0.53}Ba_{0.47})_{2.5-0.5x}Na_xNb_5O_{15}$ ($0.0 \leq x \leq 2.5$) (SBNN) ceramic. The introduction of Na^+ at A-site reduces vacancies in the structure and increases BO_6 octahedron distortion degree, which is beneficial for improving the electrical properties of SBNN ceramics [35]. Wu et al reported that for $Ba_{4-x}Sr_xSmFe_{0.5}Nb_{9.5}O_{30}$ ceramics the equivalent circuit used to describe the electrical properties of the material consists of two branches in the series, representing the electrical properties of the grain and of the grain boundary. However, a higher concentration of Sr^+ will result in a decrease in the proportion of Fe^{2+} and that the oxygen defects also decrease [36]. A TTB family of composition $Ba_6M^{3+}Nb_9O_{30}$, where ($M = Ga^{3+}$, Sc^{3+}, In^{3+}) has been reported by Rotaru & Morrison. They have concluded from the activation energy values of the electrical conduction process for $Ba_6GaNb_9O_{30}$ and $Ba_6InNb_9O_{30}$ that the conduction mechanisms are dominated by the bulk response, while for $Ba_6ScNb_9O_{30}$ the grain boundary effects mix strongly with the bulk response making it hard to clearly assign a specific grain boundary contribution [37].

The present work is focused on the titanium-zinc substitution, for compounds of global composition $Ba_5CaTi_{2-x}Zn_xNb_8O_{30}$ (x=0, 0.04, and 0.08) synthesized by standard solid-state reaction. The aims of the present work are: (i) to study the structural modifications induced by Zn substitution, (ii) to investigate the dielectric properties of ceramics samples (relative permittivity, dielectric losses, conductivity, relaxation phenomena) as a function of the Zn content in order to understand the relationships between structure, microstructure and properties.

2. Materials and methods

$Ba_5CaTi_{2-x}Zn_xNb_8O_{30}$ powders (x=0, 0.04 and 0.08) were synthesized by a classical solid-state route. The raw materials are $BaCO_3$ (Sigma-Aldrich 99%), $CaCO_3$ (Aldrich 99.9%), Nb_2O_5 (Aldrich 99.9%), ZnO (Himedia 99.9%) and TiO_2 (Sigma-Aldrich 99%). The raw powders were weighed in stoichiometric amounts and mixed in an agate mortar for 30 minutes. These powders were calcined in air at 1300 °C for 6 hours. The obtained powders were ground and mixed with polyvinyl alcohol (PVA) as a binder. Then, cylindrical pellets were obtained by pressing at 20 kN (12 mm diameter die, 2 mm thickness). The green pellets were sintered at 1450 °C for 6 hours in air. The identification of the crystalline structure of the powders was performed by X-ray diffraction (XRD) using CuKα radiation (λ=1.5406 Å) at room temperature (293 K, 0.015° step, 10–120° 2θ range, scanning speed of 1 °/min). The lattice parameters were refined by the Rietveld method using the Jana 2006 software [38]. The average crystallite size

3

"D" was estimated for the strongest diffraction peak using the Scherrer equation [39]. The density of ceramic samples was measured by using a pycnometer (AccuPyc 1340). The microstructure of the ceramic samples was checked by scanning electron microscopy (SEM) (TESCAN VEGA III LM). The average grain size of ceramic samples was estimated using Image J software. Before electrical measurements, both surfaces of the pellets were electroded using silver paste and annealed for 30 min at 300 °C to obtain good electrical contacts. The relative permittivity, dielectric losses (tan δ), the real and imaginary part of impedance and phase angle were determined using an impedance analyzer (MTZ, 10 Hz to 1 MHz).

3. Results and discussion

3.1 Structural Study

Room temperature XRD patterns of $Ba_5CaTi_{2-x}Zn_xNb_8O_{30}$ powders (x=0, 0.04 and 0.08) are shown in Fig. 1. All samples present a tetragonal tungsten bronze structure and no secondary phase is detected.
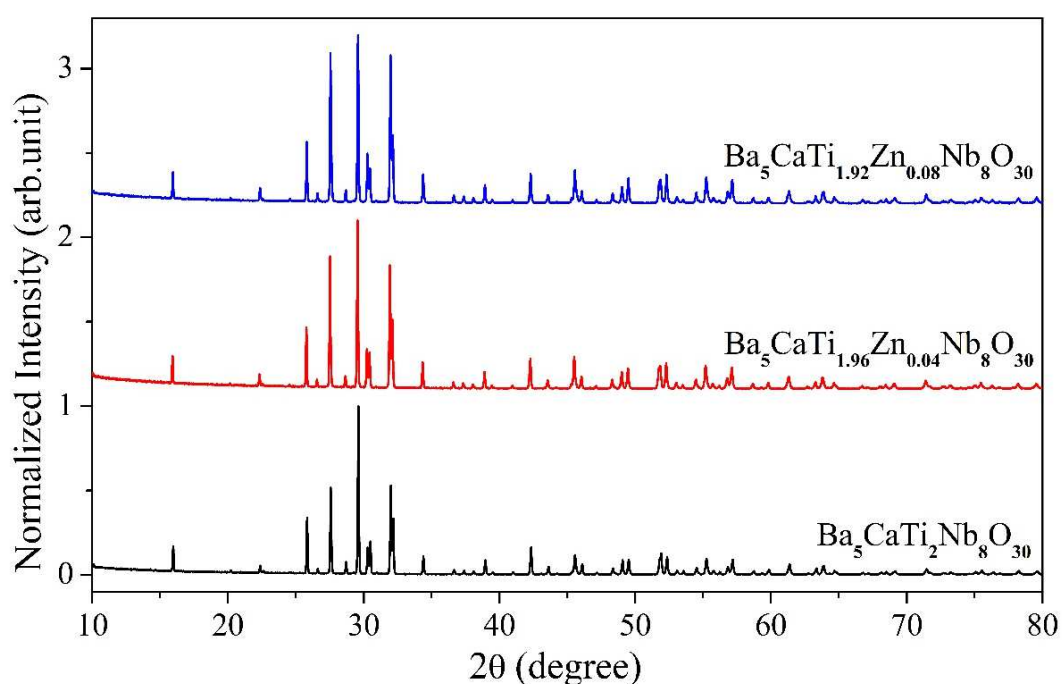

Fig. 1. XRD patterns of $Ba_5CaTi_{2-x}Zn_xNb_8O_{30}$ powders calcined at 1300 °C (x=0, 0.04 and 0.08).

The profile refinements (Le Bail) of the XRD data confirmed the tetragonal structure of the tungsten bronze, with the P4bm space group (Fig. 2). As shown in Table 1, the reliability parameters (R_{wp} and R_p) indicate a good agreement between the experimental and calculated

data, thus confirming the structural model. The refined cell parameters, crystallite size "D", and experimental conditions are presented in Table 1.
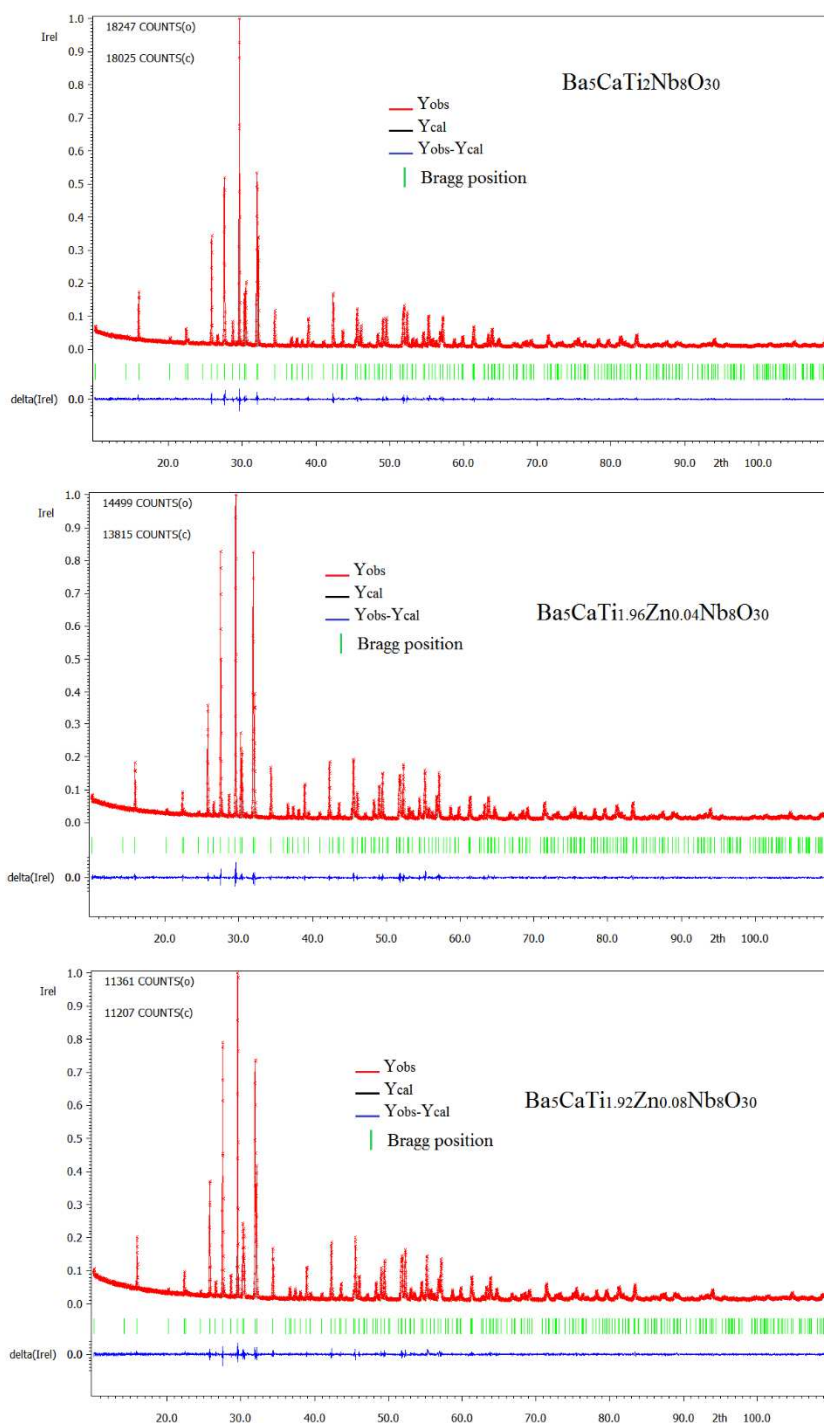

Fig. 2. Results of Rietveld refinements for $Ba_5CaTi_{2-x}Zn_xNb_8O_{30}$ powders.

Fig. 3 presents the crystallographic structure along the c-axis for the composition $Ba_5CaTi_{1.92}Zn_{0.08}Nb_8O_{30}$.
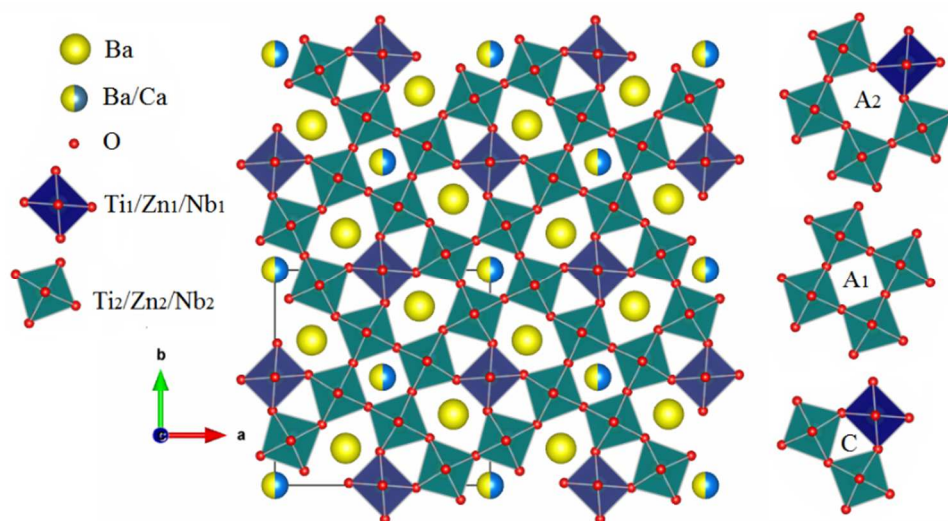
5

Fig. 3. Representation of the TTB structure of $Ba_5CaTi_{1.92}Zn_{0.08}Nb_8O_{30}$ along the "c" axis.

Table 1. Experimental parameters for X-ray powder diffraction of $Ba_5CaTi_{2-x}Zn_xNb_8O_{30}$.

Chemical formula	$Ba_5CaTi_2Nb_8O_{30}$	$Ba_5CaTi_{1.96}Zn_{0.04}Nb_8O_{30}$	$Ba_5CaTi_{1.92}Zn_{0.08}Nb_8O_{30}$
a (Å)	12.4618(5)	12.4684(3)	12.4670(4)
b (Å)	12.4618(5)	12.4684(3)	12.4670(4)
c (Å)	3.98378(15)	3.98562(11)	3.98393(12)
V (Å³)	618.67(4)	619.61(3)	619.20(3)
D (nm)	81.87	85.60	89.18
Temperature	25 °C	25 °C	25 °C
Space group	P4bm	P4bm	P4bm
Symmetry	Tetragonal	Tetragonal	Tetragonal
Rp (%)	5.49	5.40	5.71
Rwp (%)	7.55	7.25	7.84
GOF	1.47	1.31	1.53

6

3.2. Density and microstructure of ceramic samples

The relative density (ρ_r) of $Ba_5CaTi_{2-x}Zn_xNb_8O_{30}$ ceramics was calculated using the following equation [36, 39]:

$$\rho_r = \rho_m/\rho_t \tag{1}$$

The relative density ρ_r is the ratio of measured density ($\rho_m = m/v$) and the theoretical density ($\rho_t = ZM/V_0N_A$), where m, v, M, V_o and N_A are the mass of pellet, volume of pellet, molar mass, volume of unit cell and Avogadro's constant.

The densities of $Ba_5CaTi_{2-x}Zn_xNb_8O_{30}$ ceramics are listed in Table 2. The relative densities for $Ba_5CaTi_{2-x}Zn_xNb_8O_{30}$ ceramics are 95.8%, 97.2%, and 97.0% respectively, indicating that all samples are well densified.

Table 2. The theoretical, calculated and relative densities of $Ba_5CaTi_{2-x}Zn_xNb_8O_{30}$ ceramics.

Composition (x)	ρ_m (g/cm^3)	ρ_t (g/cm^3)	ρ_r (%)
0.0	5.262	5.490	95.8
0.04	5.330	5.484	97.2
0.08	5.326	5.489	97.0

The microstructural study of $Ba_5CaTi_{2-x}Zn_xNb_8O_{30}$ pellets sintered at 1450 °C for 6 hours are represented in Fig. 4, together with the results of grain size analysis. The absence of voids suggests that the samples have a high density, in agreement with the measured relative densities. The histograms of Fig. 4 indicate that the average grain sizes for $Ba_5CaTi_{2-x}Zn_xNb_8O_{30}$ (x=0, 0.04 and 0.08) are respectively 1.31, 1.49 and 1.58 μm. These mean values are logically a little bit higher than the "D" values determined by the Scherrer method. Indeed, on one hand, this method gives only rough values. On another hand, the calculated values correspond to the size of the coherent diffracting domains, which is different from the true grain size.
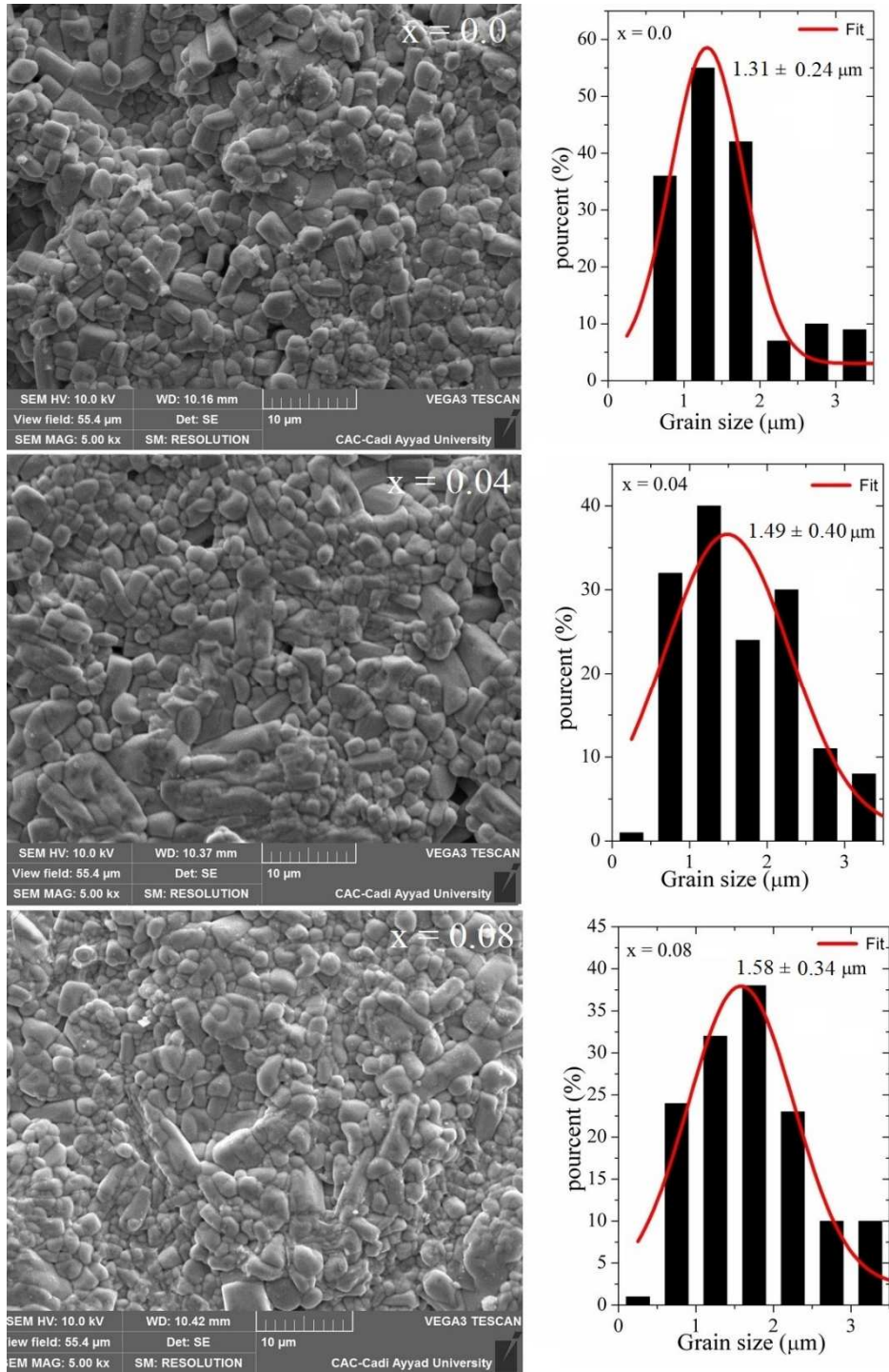
Fig. 4. SEM images of the surface of $Ba_5CaTi_{2-x}Zn_xNb_8O_{30}$ ceramics (x=0, 0.04 and 0.08) and associated grain size distributions.

3.3 Study of dielectric properties

Complex impedance spectroscopy is a non-destructive technique allowing the determination of the relationships between dielectric properties, structure and microstructure. The complex permittivity ε^* can be expressed in terms of real value (ε') and imaginary part (ε'').

$$\varepsilon^* = \varepsilon' - j\varepsilon'' \; ; \quad |\varepsilon^*| = \sqrt{(\varepsilon')^2 + (\varepsilon'')^2} \tag{2}$$

In this study, the relative permittivity (dielectric constant ε_r) and the dielectric losses ($\tan\delta$) were determined from complex impedance Z^* data ($Z^* = Z' + jZ''$) using the following expressions [40]:

$$\varepsilon' = \frac{t}{\omega.A.\varepsilon_0} \cdot \frac{-Z''}{(Z')^2 + (Z'')^2} \; ; \quad \varepsilon'' = \frac{t}{\omega.A.\varepsilon_0} \cdot \frac{Z'}{(Z')^2 + (Z'')^2} \; ; \quad \tan\delta = \frac{\varepsilon''}{\varepsilon'} \tag{3}$$

Where, $\omega = 2\pi f$ with f=frequency (Hz), A=pellet area (m^2), t=pellet thickness (m), ε_0 vacuum permittivity ($\varepsilon_0 = 8.85 \times 10^{-12}$ F.m^{-1}), Z'=real part of the impedance and Z''=imaginary part of the impedance.

Fig. 5(a-b-c) shows the variation of the relative permittivity as a function of frequency for different temperatures. The relative permittivity presents high values in the low frequency range for all temperatures. As the frequency increases, the relative permittivity decreases and reaches a plateau which only presents limited dependence on the frequency. This behavior indicates the occurrence of charged species (grain boundaries effect, oxygen vacancies…) which are unable to follow the variation of the applied alternating electric field for high frequencies. As the temperature increases, the amplitude of the dielectric constant also increases, because an increase in temperature favors the orientation of the related dipoles. Therefore, the dielectric constant increases with increasing temperature [41]. However, the origin of this behavior must be identified by complex impedance spectroscopy, in terms of analysis of the real and imaginary part of the complex impedance, analysis of the AC conductivity and study of the dielectric modulus.

Fig. 5(d) presents the relative permittivity of Ba$_5$CaTi$_{2-x}$Zn$_x$Nb$_8$O$_{30}$ ceramics at 420 °C. The relative permittivity of Ba$_5$CaTi$_{2-x}$Zn$_x$Nb$_8$O$_{30}$ with (x=0, 0.04, and 0.08) ceramics decrease with the increasing Zn^{2+} content, their value being respectively 816.04, 750.40, and 682.60 at 1 kHz.
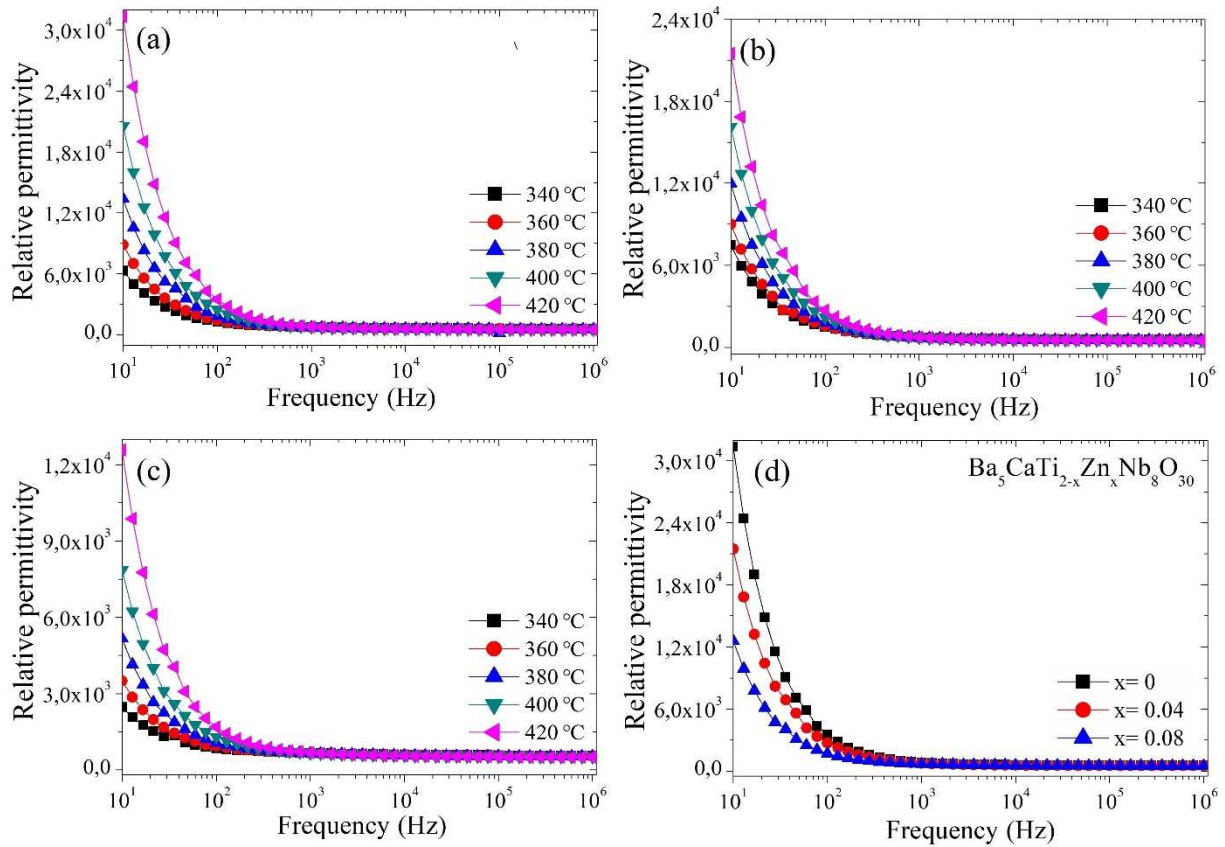
Fig. 5. Relative permittivity at different temperatures for different Zn contents in Ba$_5$CaTi$_{2-x}$Zn$_x$Nb$_8$O$_{30}$ ceramics: (a) x=0, (b) x=0.04, (c) x=0.08 and (d) comparison of relative permittivity for different values of x in Ba$_5$CaTi$_{2-x}$Zn$_x$Nb$_8$O$_{30}$ at 420 °C.

The evolution of tan (δ) values as a function of frequency for different temperatures is represented in Fig. 6(a-b-c). The tan (δ) values for Ba$_5$CaTi$_{2-x}$Zn$_x$Nb$_8$O$_{30}$ ceramics has the same behavior as the dielectric constant, i.e. tan (δ) values decrease with increasing frequency, to reach a fixed value at high frequency. This behavior for dielectric losses can be explained by the phenomenon of dipole relaxation [42]. The increase in dielectric loss values as a function of temperature may be due to thermally activated charge carriers.

Fig. 6(d) illustrates the tan(δ) values for Ba$_5$CaTi$_{2-x}$Zn$_x$Nb$_8$O$_{30}$ ceramics at 420 °C as a function of frequency. The tan(δ) values are considerably reduced for Zn-rich compositions, e.g. at 1 kHz, a value of 0.26 is observed for Ba$_5$CaTi$_{2-x}$Zn$_x$Nb$_8$O$_{30}$ with x=0.08, which is 58% smaller than for pure Ba$_5$CaTi$_2$Nb$_8$O$_{30}$, suggesting that the introduction of Zn into the ceramic decreases dielectric losses.

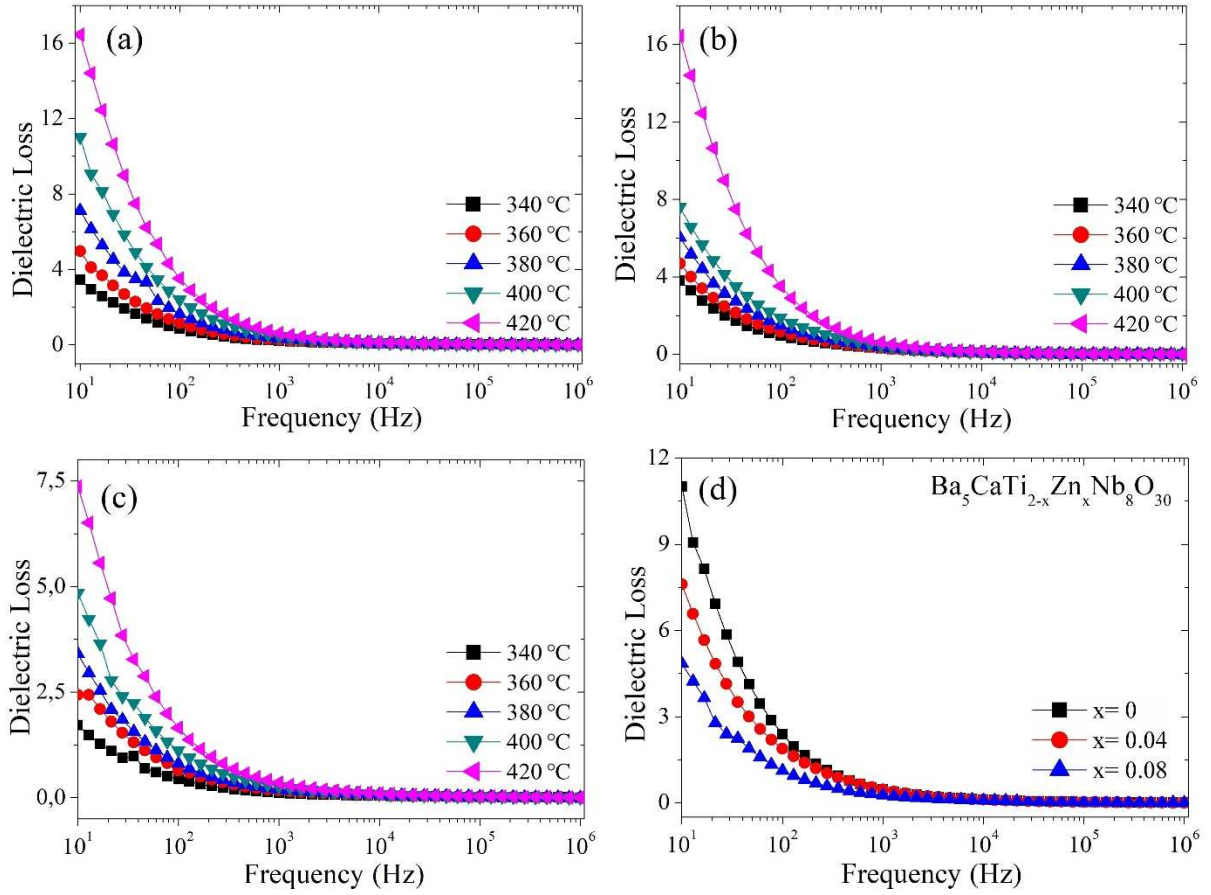Fig. 6. Dielectric losses (tan δ) at different temperatures for different Zn contents in Ba$_5$CaTi$_{2-x}$Zn$_x$Nb$_8$O$_{30}$; (a) x=0, (b) x=0.04, (c) x=0.08 and (d) comparison of Dielectric losses (tan δ) for different values of x in Ba$_5$CaTi$_{2-x}$Zn$_x$Nb$_8$O$_{30}$ at 420 °C.

3.4 Complex Impedance Analysis (CIA)

CIA using Nyquist plots allows the understanding of grains, grain boundaries and possible electrode effects on the capacitive, reactive, resistive and inductive properties of materials. A Nyquist diagram is a plot of the Z" imaginary part of the impedance as a function of the real part Z'. Fig. 7 shows Nyquist plots for Ba$_5$CaTi$_{2-x}$Zn$_x$Nb$_8$O$_{30}$ ceramics (x=0, 0.04 and 0.08) at different temperatures, and a comparison of the diagrams at 420 °C for the different Zn contents. As expected, the diagrams appear as more or less as semicircles, with their center above the real axis. With increasing temperatures, these semicircles become more complete in the measured frequency range (10Hz-1MHz). Since the intersection of the semicircle on the real axis (Z') directly corresponds to the global circuit resistance "R", this value has a marked effect on the magnitude of real and imaginary part of the impedance [43]. Logically, the plots (Fig. 7) evidence that the radius of the semicircle decrease, i.e. the resistance decreases with increasing temperature for a given "x" value.

11
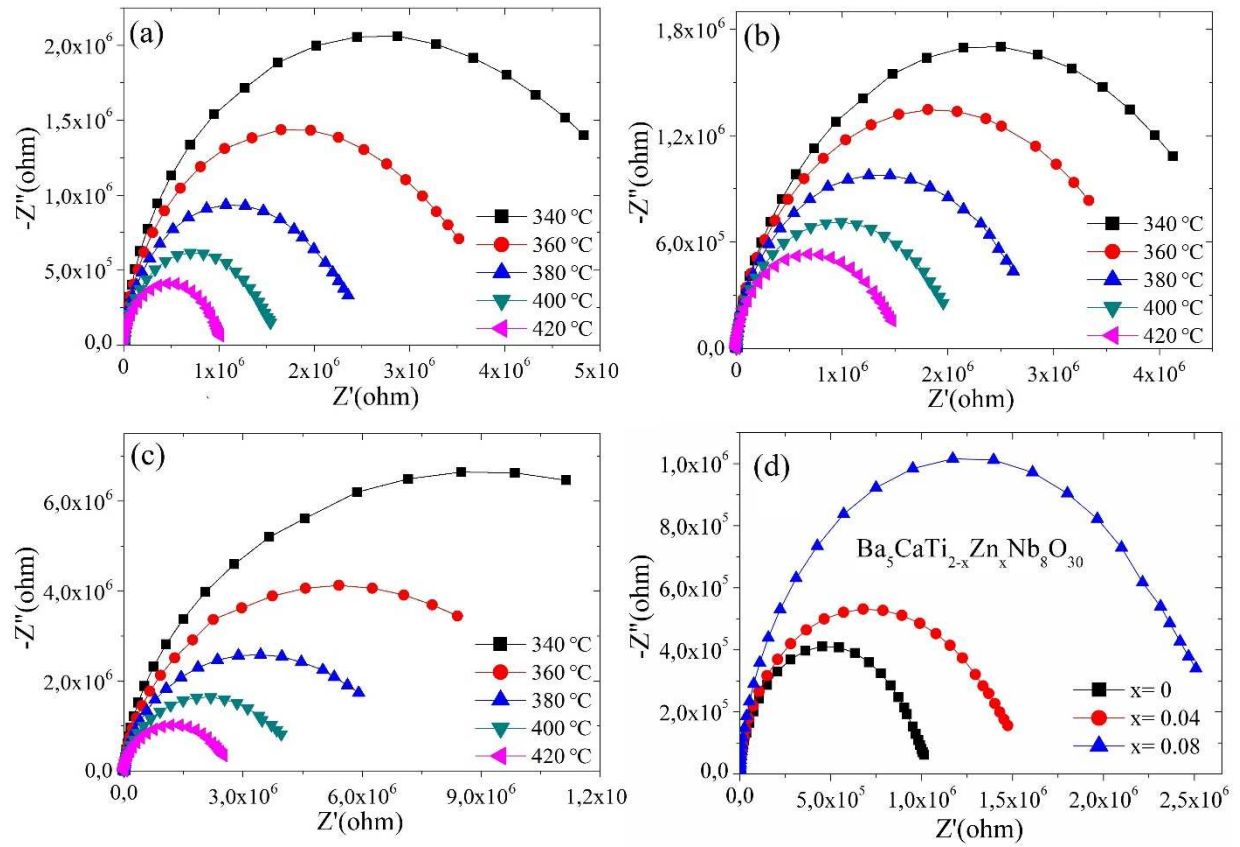
Fig. 7. Complex impedance diagram at different temperatures for different Zn contents in $Ba_5CaTi_{2-x}Zn_xNb_8O_{30}$; (a) x=0, (b) x=0.04, (c) x=0.08 and (d) comparison of the diagrams for different values of x in $Ba_5CaTi_{2-x}Zn_xNb_8O_{30}$ at 420 °C.

However, the simulation of the experimental data with the appropriate equivalent electrical circuit (ZView software), revealed that the data correspond well to the series connection of two cells, associated respectively to grains and grain boundaries effects. The appropriate equivalent circuit is presented in Fig. 8 for the $Ba_5CaTi_{1.96}Zn_{0.04}Nb_8O_{30}$ composition (x=0.04).

Fig. 8. Adjusted Nyquist diagram for the $Ba_5CaTi_{1.96}Zn_{0.04}Nb_8O_{30}$ composition (x=0.04) at different temperatures. The solid red lines show the data adjusted with the ZView software.

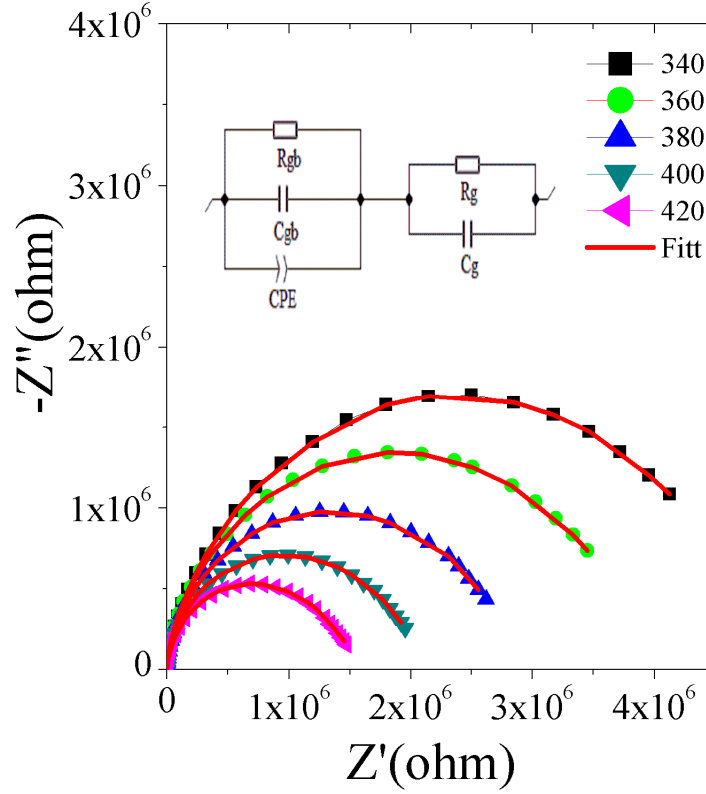In the first parallel circuit, associated to the grain contribution, R_g and C_g correspond to the grain resistance and the grain capacitance. In the second parallel circuit, R_{gb}, C_{gb} and CPE are grain boundary resistance, grain boundary capacitance and constant phase element. A constant phase element (CPE) is introduced into the second circuit, due to the non-ideal capacitive behavior. This non-ideal grain boundary behavior can be due to the presence of more than one relaxation process [44]. The constant phase element (Q) is evaluated by the following relationship [30, 40, 45, 46]:

$$C = (R^{1-\alpha}Q)^{1/\alpha} \tag{4}$$

In this case, $Z_{CPE} = \frac{1}{Q(j\omega)^\alpha}$ where ω is the angular frequency (rad/s), $j = \sqrt{-1}$. Q is the CPE parameter which gives the value of the capacitance of the constant phase element (CPE), and has the magnitude of $\frac{1}{Z_{CPE}}$ at ω = 1 rad/s with units $|Fs^{\alpha-1}|$. The fitting process also gives the value of the depression angle $\beta = \frac{\pi}{2}(1-\alpha)$ [47].

For an ideal resistor and an ideal capacitor, the "α" values are respectively zero and one [48]. The experimental data were thus modeled with this equivalent circuit using ZView software. A good agreement between the experimental data and the calculated values gives us

13

confidence in the proposed equivalent circuit. The various adjusted parameters are presented in Table 3.

Table 3. Equivalent circuit electrical parameters obtained from a complex impedance spectrum for $Ba_5CaTi_{2-x}Zn_xNb_8O_{30}$ ceramics.

	T (°C)	R_{gb} (MΩ)	C_{gb} (nF)	Q (nF.s$^{\alpha-1}$)	α	R_g (KΩ)	C_g (nF)	β (°)
x=0	340	4.8156	0.3280	6.755	0.47934	1.898	6.591	23.429
	360	3.9307	0.3057E	5.173	0.52426	1.430	8.227	21.408
	380	2.5895	0.2883	5.194	0.53831	1.241	1.0649	20.776
	400	1.636	0.2751	4.970	0.55136	1.071	1.2716	20.188
	420	1.0592	0.2653	4.865	0.56029	0.905	1.5431	19.786
x=0.04	340	6.479	0.3451	4.101	0.60956	199.26	1.493	17.569
	360	4.1192	0.3231	5.568	0.56419	178.23	1.719	19.611
	380	2.7942	0.3103	6.035	0.55649	152.01	1.718	19.957
	400	2.0689	0.3004	8.805	0.52761	145.04	1.708	21.257
	420	1.4928	0.2920	9.894	0.52204	121.96	1.686	21.508
x=0.08	340	17.511	0.3010	1.618	0.63889	376.54	4.166	16.249
	360	11.165	0.2871	2.185	0.6203	324.51	4.413	17.086
	380	6.9887	0.2783	2.818	0.60887	298.55	3.871	17.601
	400	4.441	0.2711	3.796	0.59005	245.59	3.502	18.447
	420	2.5769	0.2647	4.720	0.57428	219.77	3.408	19.157

In the graph of Fig. 9, we have fitted the experimental data with the equation of the circle by taking some data sets Z′ and Z″ in the Mathematica software. Different data sets Z′ and Z″ of a specific temperature are fitted again and again to find the best fit of the semicircle and thus obtaining the center, radius and intercept of the semicircle [49]. In addition, our semicircles are not perfect, they are tilted or depressed relative to the real Z′ axis. The tilting of the semicircular arcs is common in ceramic samples wherein the presence of imperfections and inhomogeneities are common resulting in the distribution in relaxation time and a deviation from the Debye

behavior [50]. These semicircular arcs were fitted with (RQC)(RC) circuit, where Q is the constant phase element.
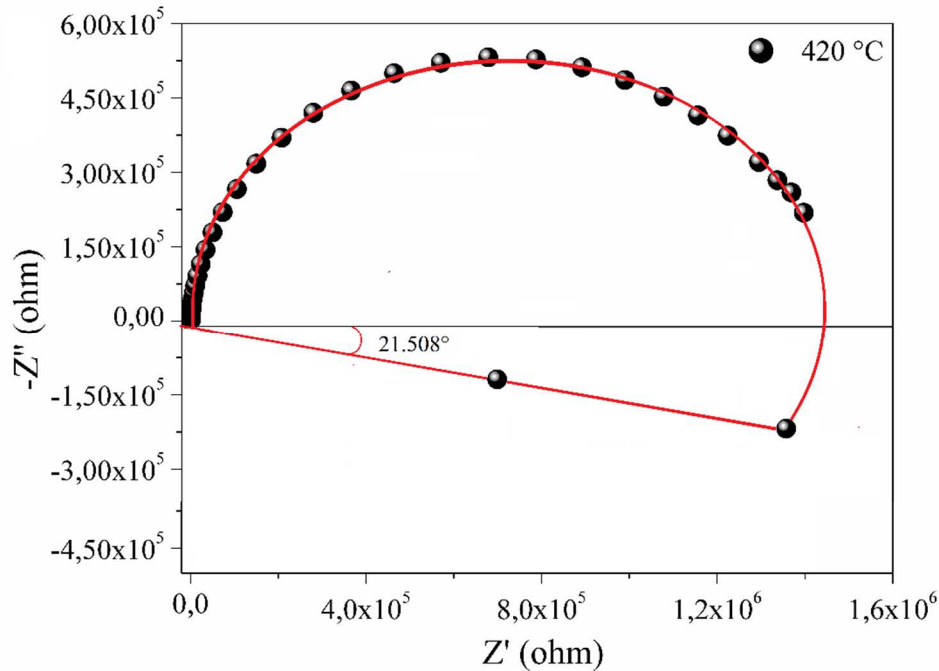

Fig. 9. Experimental verification of Nyquist plot data with the depression angle for Ba$_5$CaTi$_{1.96}$Zn$_{0.04}$Nb$_8$O$_{30}$ ceramic at 420 °C.

We have also determined the angle (depression angle β) which is a measure of the degree of deviation from the Debye behavior [51]. The contribution of the interface or electrode effect is not observed in our experimental range of frequency because it appears in the very low frequencies [52].

Table 3 shows that the values of R$_g$ and R$_{gb}$ increase with the amount of Zn incorporated in the tungsten bronze lattice. The increase in grain resistance with the addition of Zn may be due to the increase in grain size in the Ba$_5$CaTi$_{2-x}$Zn$_x$Nb$_8$O$_{30}$ ceramics (Fig. 4), while the increase in grain boundary resistance may be due to the decrease of grain boundary surface area with the addition of Zn.

In another way, the values of R$_g$ and R$_{gb}$ decrease with the increasing temperatures for all Ba$_5$CaTi$_{2-x}$Zn$_x$Nb$_8$O$_{30}$ ceramics, showing the occurrence of a thermally activated conduction mechanisms in the grains and at the grain boundaries.

The values of grain and grain boundary resistances obtained from Nyquist plots (Fig. 7) were analyzed using the following Arrhenius' law to evaluate their activation energy [53].

15

$$R = R_0 \exp(-Ea/k_B T) \tag{5}$$

Where Ea is the activation energy for conduction, k_B is the Boltzmann's constant, R_0 is the pre-exponential factor and T the temperature (K). The E_g and E_{gb} values obtained by linear fitting with the above equation are presented in Fig. 10, and the results are reported in Table 4.
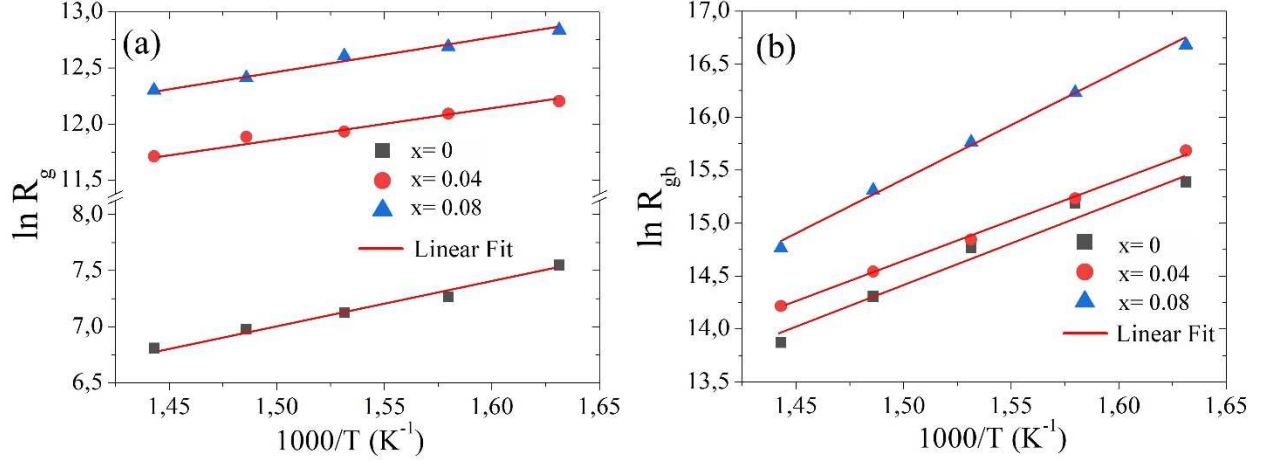

Fig. 10. Arrhenius plot of the data obtained for $Ba_5CaTi_{2-x}Zn_xNb_8O_{30}$ ceramics from the results of impedance circles: (a) for grain, and (b) for grain boundaries.

The grain activation energies are between 0.217 and 0.324 eV and grain boundary activation energies between 0.664 and 0.868 eV, for temperatures between 340 °C and 420 °C. The higher activation energy values for the grain boundaries are probably related to the more disordered nature of the grain boundaries.

Table 4. Values of activation energies for $Ba_5CaTi_{2-x}Zn_xNb_8O_{30}$ ceramics obtained from the fitting of the curves of Fig. 10.

Composition (x)	Ea/eV (grain)	Ea/eV (grain boundary)
0.0	0.324	0.711
0.04	0.217	0.664
0.08	0.247	0.868

3.5. A.C. Conductivity

Conductivity values were calculated from the dielectric data using the relationship:

$$\sigma_{AC} = \omega \varepsilon_0 \varepsilon_r \tan\delta \tag{6}$$

Where ε_o, ε_r, $\tan(\delta)$, ω, and σ_{AC} are respectively vacuum permittivity, relative permittivity, dielectric losses, angular frequency and AC conductivity.
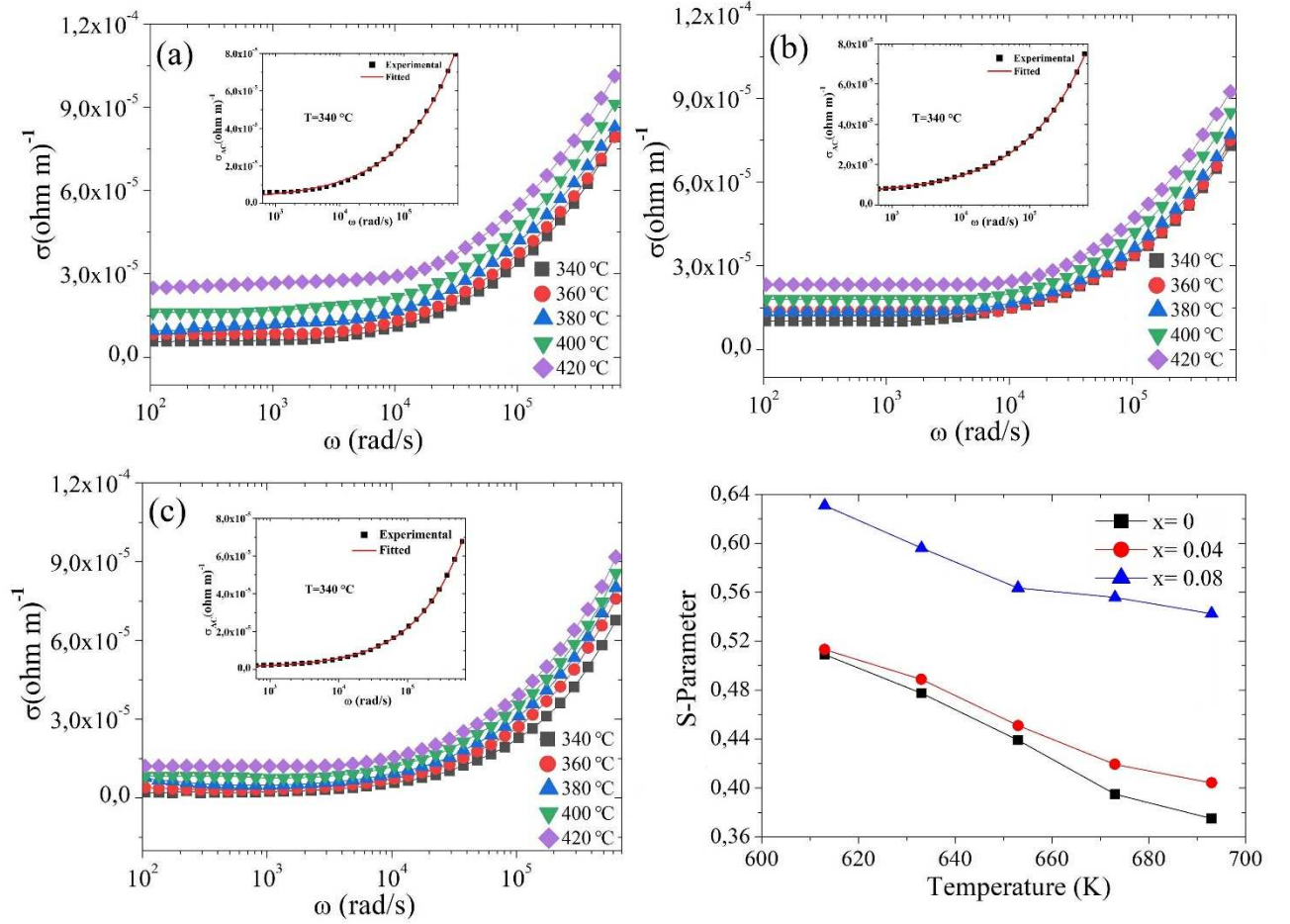
16

Fig. 11. AC conductivity as a function of frequency at different temperatures for Ba$_5$CaTi$_{2-x}$Zn$_x$Nb$_8$O$_{30}$ ceramics; (a) x=0, (b) x=0.04, (c) x=0.08 and (d) variation of the "s" parameter with temperature for Ba$_5$CaTi$_{2-x}$Zn$_x$Nb$_8$O$_{30}$ ceramics.

The AC conductivity (Fig. 11 a-b-c) increases with increasing frequency for all temperatures. The AC conductivity at each measured temperature presents two separate regions. For low frequencies, a first region is observed where the conductivity does not change with frequency. For the second region, the conductivity increases with increasing frequency. This type of AC conductivity can be explained by Jonscher's power law [54, 55].

$$\sigma_{AC} = \sigma_{DC} + A\omega^s \qquad (7)$$

Where the σ_{DC} indicates the DC conductivity and the second term is the frequency dependent AC conductivity. "A" is known as the polarizability force and "s" is the temperature dependent parameter. The variation of the "s" parameter with temperature is used to determine conduction mechanism. Funke has explained [56] the physical meaning of the numerical values of the "s" parameter. s ≤ 1 means that the hopping motion involves a translational motion with a sudden hopping, whereas s > 1, means that the motion involves localized hopping without the species leaving the neighborhood. The insets of Fig. 11(a-b-c) show the nonlinear curve fit to Jonscher's

17

power law for $Ba_5CaTi_{2-x}Zn_xNb_8O_{30}$ at 340 °C. The fitting parameters A, s, and σ_{DC} were calculated from the nonlinear fitting (Table 5). Fig. 11(d) shows the variation of "s" with temperature (340-420 °C), demonstrating that "s" is varying inversely with temperature. This observation confirms that correlated barrier hopping (CBH) is the appropriate model to understand charge transport mechanism in these samples [57]. Thus, according to this model, AC conductivity in all the samples is due to the hopping of charge carriers between two sites over the potential barrier separating them, because of thermal activation [58].

Table 5. Parameters obtained from Joncher's plot for $Ba_5CaTi_{2-x}Zn_xNb_8O_{30}$ ceramics.

	Temperature (°C)	s	A ($\Omega^{-1}m^{-1}rad^{-s}$)	σ_{DC} (Ω m)$^{-1}$	(R^2)
x=0	340	0.50893	8.74044×10^{-8}	2.22745×10^{-6}	0.99886
	360	0.47747	1.32042×10^{-7}	3.55384×10^{-6}	0.99661
	380	0.43897	2.32918×10^{-7}	3.97773×10^{-6}	0.99809
	400	0.39492	4.52137×10^{-7}	3.97839×10^{-6}	0.98461
	420	0.37487	6.4152×10^{-7}	6.195×10^{-6}	0.99977
x=0.04	340	0.51315	7.15154×10^{-8}	4.51721×10^{-6}	0.98768
	360	0.48872	9.87002×10^{-8}	5.96364×10^{-6}	0.99992
	380	0.45095	1.76763×10^{-7}	6.70268×10^{-6}	0.99973
	400	0.4193	3.0135×10^{-7}	8.69866×10^{-6}	0.99927
	420	0.40411	4.00179×10^{-7}	1.12502×10^{-7}	0.99881
x=0.08	340	0.63082	1.47775×10^{-8}	9.17883×10^{-7}	0.99986
	360	0.59609	2.63396×10^{-8}	1.1985×10^{-6}	0.99964
	380	0.56356	4.25835×10^{-8}	2.10108×10^{-6}	0.99936
	400	0.55585	4.90312×10^{-8}	4.39909×10^{-6}	0.99876
	420	0.54256	6.10214×10^{-8}	6.93179×10^{-6}	0.9992

From Table 5, it can be seen that with the rise in temperature, the strength of polarizability (A) increases, as confirmed by dielectric constant values of Fig. 5.

Fig. 12 shows the variation of $\ln(\sigma_{DC})$ with the inverse of the temperature ($10^3/T$), which gives the value of the activation energy for the electrical conduction of $Ba_5CaTi_{2-x}Zn_xNb_8O_{30}$ ceramics at 1 kHz, calculated by Arrhenius' law.

$$\sigma_{DC} = \sigma_0 \exp(-Ea/k_BT) \tag{8}$$

Where k_B is the Boltzmann constant, σ_o is the pre-exponential factor, T is the temperature (K) and Ea is the activation energy. The experimental data were fitted with the above equation (Fig. 12) and the results of the fit are reported in Table 6. For $Ba_5CaTi_{2-x}Zn_xNb_8O_{30}$ ceramics, two activation energies were obtained, which corresponds respectively to grains and grain boundaries. It should be noted that the activation energy of the grain boundaries is higher than that of the grains. This means again that the grain boundaries have a higher resistance than the grains, as previously obtained from Nyquist plots (see Table 3).
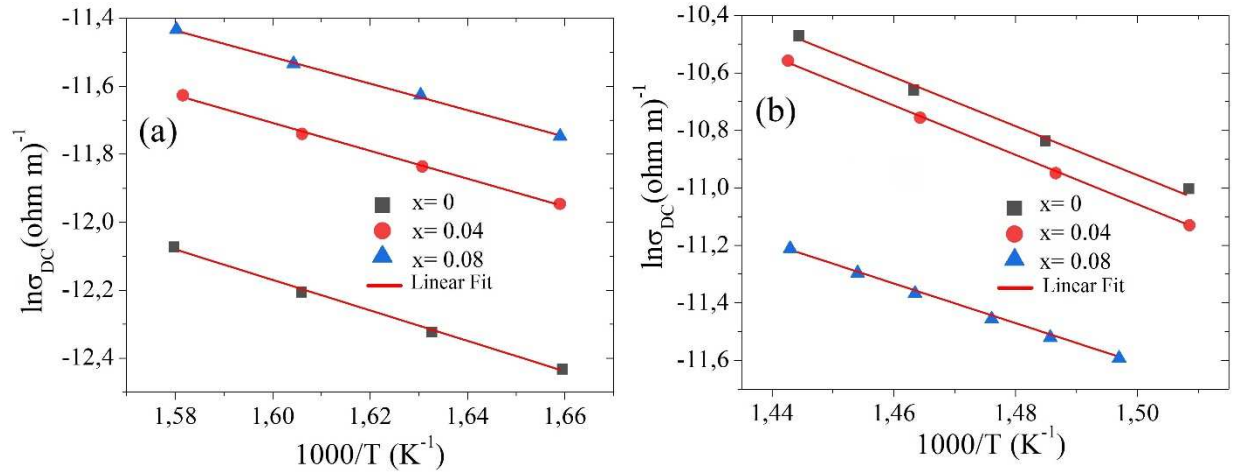

Fig. 12. Conductivity $\ln(\sigma_{DC})$ as a function of 1000/T for $Ba_5CaTi_{2-x}Zn_xNb_8O_{30}$ ceramics; (a) for grain, and (b) for grain boundaries at 1 kHz.

In ferroelectric oxides, the thermal activation energy is closely related to the concentration of oxygen vacancies (OVs). For $Ba_5CaTi_{2-x}Zn_xNb_8O_{30}$ ceramics, the creation of oxygen vacancies is due to the substitutions of Ti^{4+}, which is tetravalent, by Zn^{2+} which is bivalent. This heterogeneous substitution leads to the creation of oxygen vacancies.

Table 6. Values of activation energy for $Ba_5CaTi_{2-x}Zn_xNb_8O_{30}$ obtained from DC conductivity measurement at 1kHz.

Composition (x)	Ea/eV (grain)	Ea/eV (grain boundary)
0.0	0.387	0.748
0.04	0.353	0.713
0.08	0.340	0.609

According to Table 6, the activation energies of grains and grain boundaries for $Ba_5CaTi_{2-x}Zn_xNb_8O_{30}$ ceramics decreases with increasing Zn content. For a stoichiometric perovskite ABO_3, the activation energy is Ea = 2eV, while the value of Ea is lowered to 1eV for $ABO_{2.95}$

and 0.5eV for ABO$_{2.90}$ [59, 60]. Furthermore, it is known that the most mobile ionic species in the perovskite tungsten bronze lattice are the single and double ionized OVs. It was frequently reported that the activation energy of single ionized OVs is about 0.3-0.5 eV and about 0.6-1.2 eV for doubly ionized OVs. Our Ea results for grains (0.340-0.387eV) are very close to the activation energy of ionic conductivity induced by single ionized OVs, while the Ea values for grain boundaries (0.609-0.748eV) are very close to the activation energy of ionic conductivity induced by doubly ionized OVs in perovskite and tungsten bronze type ferroelectric oxides reported by many authors [36, 61-66]. The observed decrease of the activation energies values of the grains and the grain boundaries (Table 6) indicates that the oxygen vacancies (OVs) induced by the Zn substitution are probably responsible for conduction mechanism in the Ba$_5$CaTi$_{2-x}$Zn$_x$Nb$_8$O$_{30}$ ceramics. Therefore, we can reasonably conclude that the conducting species in Ba$_5$CaTi$_{2-x}$Zn$_x$Nb$_8$O$_{30}$ ceramics are single and doubly ionized OVs.

Oxygen vacancies (OVs) can easily be formed in oxide materials by the loss of oxygen from the crystal lattice during heating at elevated temperatures (typically >1300 °C) [67], or in our case by the Ti^{4+}/Zn^{2+} substitution. The oxygen vacancies creation can be explained by the Kröger-Vink defect equation:

$$ZnO \xrightarrow{TiO_2} Zn_{Ti}^{//} + O_O^{\times} + V_{\ddot{O}} \tag{9}$$

The single and double ionized OVs will create the conducting electrons, written as:

$$V_O \leftrightarrow V_{\dot{O}} + e' \tag{10a}$$

$$V_O \leftrightarrow V_{\ddot{O}} + 2e' \tag{10b}$$

3.6. The spectrum of the imaginary part of the impedance

Fig. 13(a-b-c) present the variation of the imaginary part of the impedance (Z ") as a function of the frequency for Ba$_5$CaTi$_{2-x}$Zn$_x$Nb$_8$O$_{30}$ compositions at different temperatures. Temperature dependent peaks appear in the frequency-dependent Z" plot. The amplitude of Z" at the peak position is called Z"$_{max}$ and the corresponding frequency (f$_{max}$) is known as the relaxation frequency. The relaxation frequency (f$_{max}$) is small at low temperatures; this means that moving load carriers (OVs) take a long time to move from one site to another. The value of Z"$_{max}$ decreases with increasing temperature; whereas f$_{max}$ is shifted to higher frequencies with increasing temperature. This displacement of the maximum frequency to higher frequencies implies that the relaxation time "τ" decreases with increasing temperature $(2\pi f_{max}^{Z''} \tau_{Z''} = 1)$.

Fig. 13(d) shows the variation of the imaginary part of the impedance (Z'') as a function of the Zn content in $Ba_5CaTi_{2-x}Zn_xNb_8O_{30}$ at 420 °C. The amplitude of the Z''_{max} value increases with increasing Zn content. The significant increase in Z''_{max} values for Zn-rich compositions could be due to the increase in grains and grain boundary resistance. These results suggest that Zn doping in the $Ba_5CaTi_{2-x}Zn_xNb_8O_{30}$ structure has remarkably affected the electrical behavior of the ceramics.
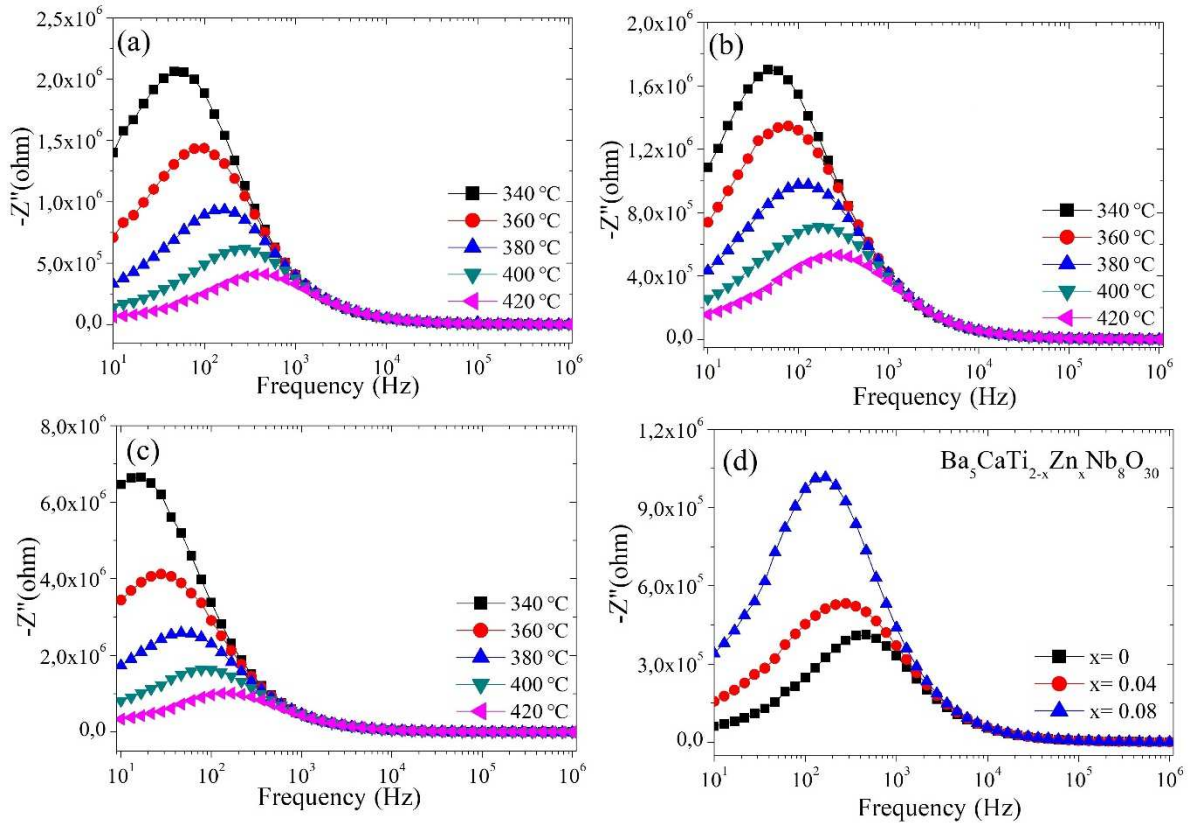

Fig. 13. Variation of the imaginary part (Z'') of the impedance with frequency at different temperatures for different concentrations of Zn in $Ba_5CaTi_{2-x}Zn_xNb_8O_{30}$; (a) x=0, (b) x=0.04, (c) x=0.08 and (d) comparison of the imaginary part (Z'') of the impedance for different values of x in $Ba_5CaTi_{2-x}Zn_xNb_8O_{30}$ at 420 °C.

3.7. The spectrum of the real part of the impedance

Fig. 14(a-b-c) presents the real part of the impedance Z' as a function of the frequency at different temperatures for $Ba_5CaTi_{2-x}Zn_xNb_8O_{30}$ ceramics. The figure shows that the values of Z' decrease with increasing frequency and converge to zero in the high-frequency region. At low frequencies, the real part of the impedance Z' for the three compounds has a high value due to the presence of multicomponent polarizations, such as electron polarization, ion polarization, orientation polarization, interfacial polarization, etc. But at higher frequency, the dipolar orientation and the interfacial polarization contributions have decreased, leading to a constant

21

value of the real part of the impedance Z' [68]. The decrease in Z' with increasing frequency and temperature indicates an increase in AC conductivity. At low frequency, the decrease in Z' with increasing temperature indicates the negative temperature coefficient of resistance (NTCR) behavior [69, 70].

Fig. 14(d) presents the variation of the real part of the impedance (Z') as a function of the Zn content in $Ba_5CaTi_{2-x}Zn_xNb_8O_{30}$ ceramics at 420 °C. The value of Z' at low frequency increases with increasing Zn content.

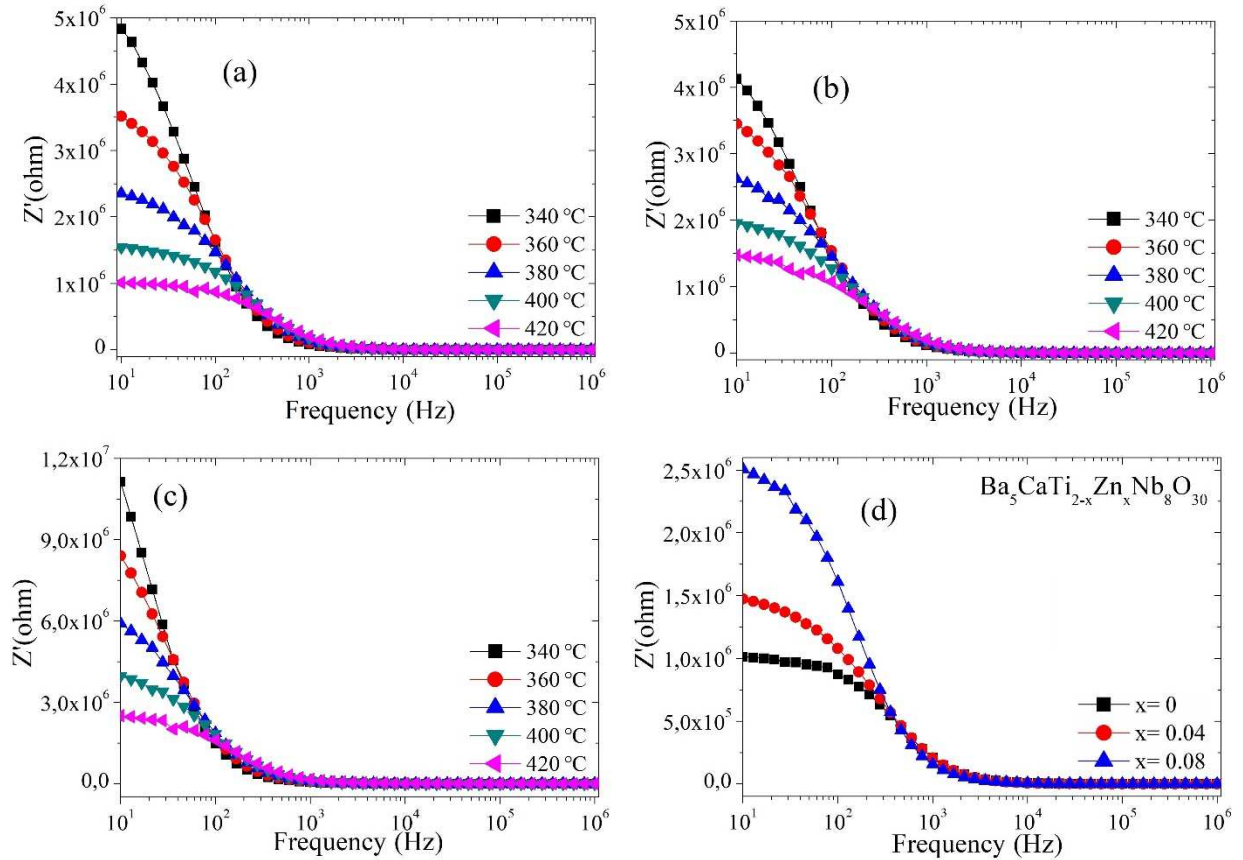Fig. 14. Real part of impedance (Z') as a function of frequency at different temperatures for $Ba_5CaTi_{2-x}Zn_xNb_8O_{30}$ ceramics; (a) x=0, (b) x=0.04, (c) x=0.08, and (d) comparison of the Real part (Z') of the impedance for different values of x in $Ba_5CaTi_{2-x}Zn_xNb_8O_{30}$ at 420 °C.

3.8. Modulus spectroscopy study

The complex analysis of the dielectric modulus is a practical tool for studying electrical transport phenomena in ceramics and for distinguishing the microscopic processes responsible for dielectric relaxation [71]. The complex dielectric modulus, M*, is given by the inverse of the complex dielectric constant.

$$M^* = 1/\mathcal{E}^* = j\omega C_0 Z^* = M' + jM''$$ (11)

Where M' and M" are respectively the real and imaginary part of the dielectric modulus, $C_0 = \frac{\varepsilon_0 A}{d}$ is the geometric capacitance (where ε_0=vacuum permittivity, A=surface, d=thickness).

The real and imaginary parts of the complex module are expressed as following:

$$M' = \frac{\varepsilon'}{\varepsilon'^2 + \varepsilon''^2}; \quad M'' = \frac{\varepsilon''}{\varepsilon'^2 + \varepsilon''^2} \tag{12}$$

Where ε' and ε'' are respectively the real and imaginary part of the dielectric permittivity.

Fig. 15 presents the variation of the real part of the modulus (M') with respect to the frequencies at different temperatures. In the lower frequency region, M' is close to zero, but with increasing frequency M' increases continuously and approaches saturation beyond a particular frequency. This frequency depends on the temperature and, consequently, the amplitude of M' saturates to a higher value as the temperature increases.
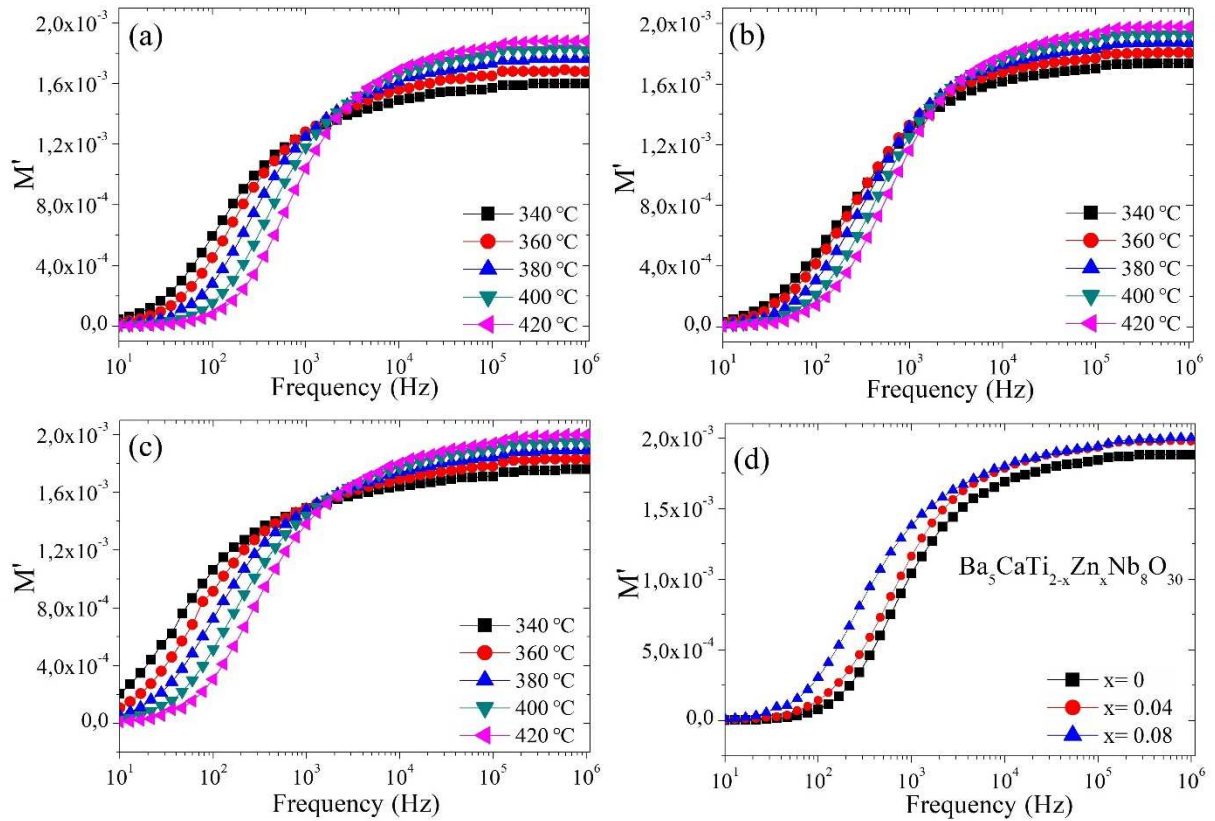

Fig.15. Real part of the modulus M' as a function of frequency at different temperatures for $Ba_5CaTi_{2-x}Zn_xNb_8O_{30}$ ceramics; (a) x=0, (b) x=0.04, (c) x=0.08 and (d) comparison of the real part of the modulus for $Ba_5CaTi_{2-x}Zn_xNb_8O_{30}$ ceramics at 420 °C.

The saturation in M' is attributed to the conduction mechanism due to the mobility of the available charge carriers (OVs) [72, 73]. However, the increase in temperature enhances the mobility of the charge carriers, so the global saturation of M' increases with temperature.

The variation of the imaginary part of the modulus M" as a function of frequency is shown in Fig. 16(a-b-c). Three types of regions are observed. The first one is the low frequency region below the maximum of the peak of the modulus M"($2\pi f_{max}^{M''}\tau_{M''} < 1$), where charge carriers can move at long distances, i.e. ions can hop from one site to the neighboring site (long-distance hopping) [74]. The second region is the high-frequency region above the peak maximum of the M" modulus ($2\pi f_{max}^{M''}\tau_{M''} > 1$), where most of the charge carriers are confined in their potential wells. They move over a short distance and can only make a localized movement inside the well [75]. The last region is at the top of the peak of M" ($2\pi f_{max}^{M''}\tau_{M''} = 1$), where the transition from long-distance to short-distance mobility occurs.
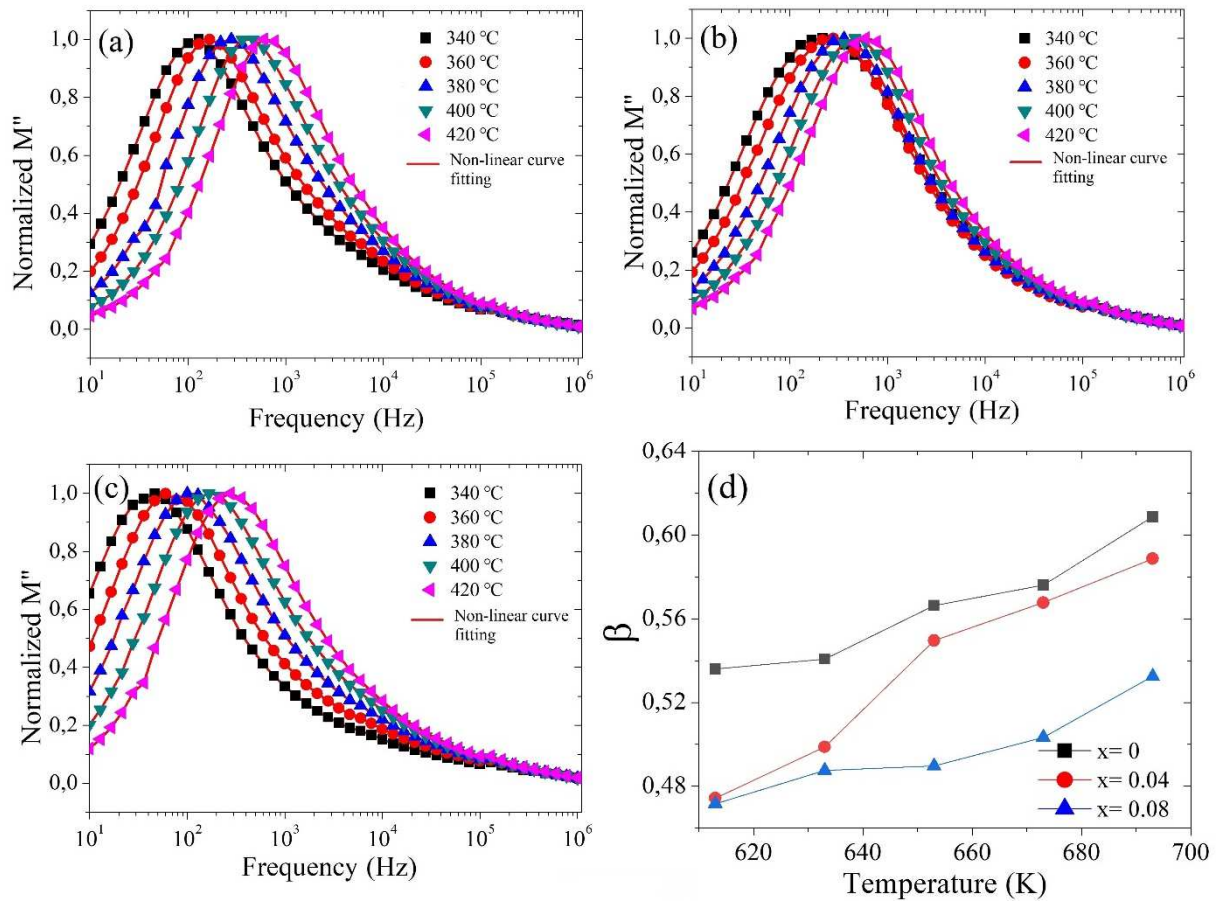

Fig. 16. Imaginary part of the modulus M" as a function of frequency at different temperatures for Ba$_5$CaTi$_{2-x}$Zn$_x$Nb$_8$O$_{30}$ ceramics; (a) x=0, (b) x=0.04, (c) x=0.08 and (d) The plot of β-parameter versus Temperature for Ba$_5$CaTi$_{2-x}$Zn$_x$Nb$_8$O$_{30}$ ceramics.

An asymmetric broadening is also observed in the relaxation peaks (M"$_{max}$), suggesting the existence of a stretched exponent parameter (β) for determining the type of relaxation process within a material, i.e. Debye or non-Debye type relaxation. To confirm this, the stretch

coefficient (β) was evaluated by fitting the imaginary part of M″ derived from the modified Kohlrausch-Williams-Watts (KWW) function proposed by Bergman [76].

$$M'' = \frac{M''_{max}}{(1-\beta) + \frac{\beta}{1+\beta}\left[\beta\left(\frac{f_{max}}{f}\right) + \left(\frac{f}{f_{max}}\right)^{\beta}\right]} \tag{13}$$

Where, M″_max is the maximum value of M″, and f_{max} is the corresponding maximum frequency. For an ideal Debye type relaxation, $\beta = 1$ and for non-Debye type relaxation, $(0 < \beta < 1)$. The results of Fig. 16(d) indicate that the value of (β) increases with increasing temperature, i.e., from β = 0.4717 to 0.6087. These results confirm that the relaxation process is non-Debye type in $Ba_5CaTi_{2-x}Zn_xNb_8O_{30}$ ceramics.

The complex modulus spectrum of M″ vs. M′ at 240 °C for the compound $Ba_5CaTi_{1.96}Zn_{0.04}Nb_8O_{30}$ gives half circles as shown in Fig. 17. The figure clearly shows two semicircles. The first semicircle at a lower frequency is due to the effect of grains, while the second semicircle at a higher frequency is due to grain boundary effect [30]. A small semicircle appears at higher frequencies, which is attributed to the electrode effect. This behavior was not visualized by the Nyquist plot (Fig. 7).
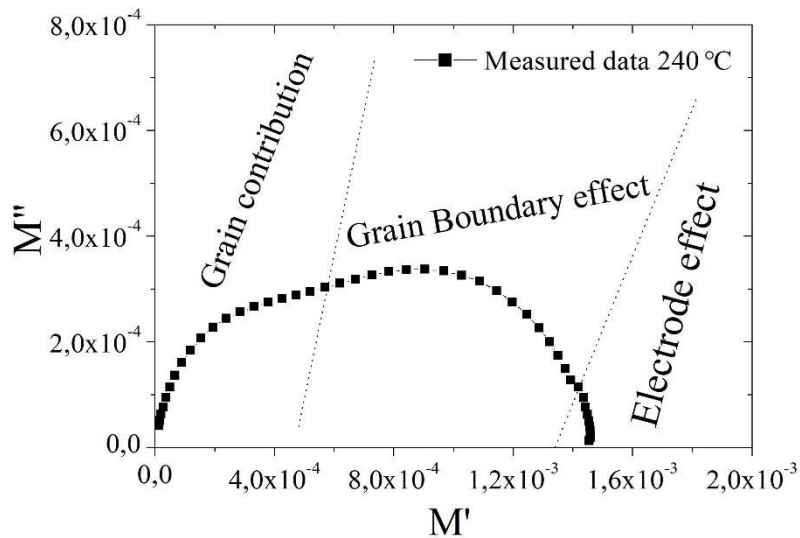

Fig. 17. Complex modulus diagram (M″ vs. M′) for $Ba_5CaTi_{1.96}Zn_{0.04}Nb_8O_{30}$ at 240 °C.

Fig. 18 shows the variation of Z″/Z″_MAX and M″/M″_MAX with frequency at 420°C for $Ba_5CaTi_{2-x}Zn_xNb_8O_{30}$ ceramics. The peak (Z″/Z″_MAX and M″/M″_MAX) do not overlap, confirming the non-Debye type relaxation behavior found from the results of the imaginary part of module as a function of frequency (Fig. 16). For all other temperatures, the same nature was found [77].
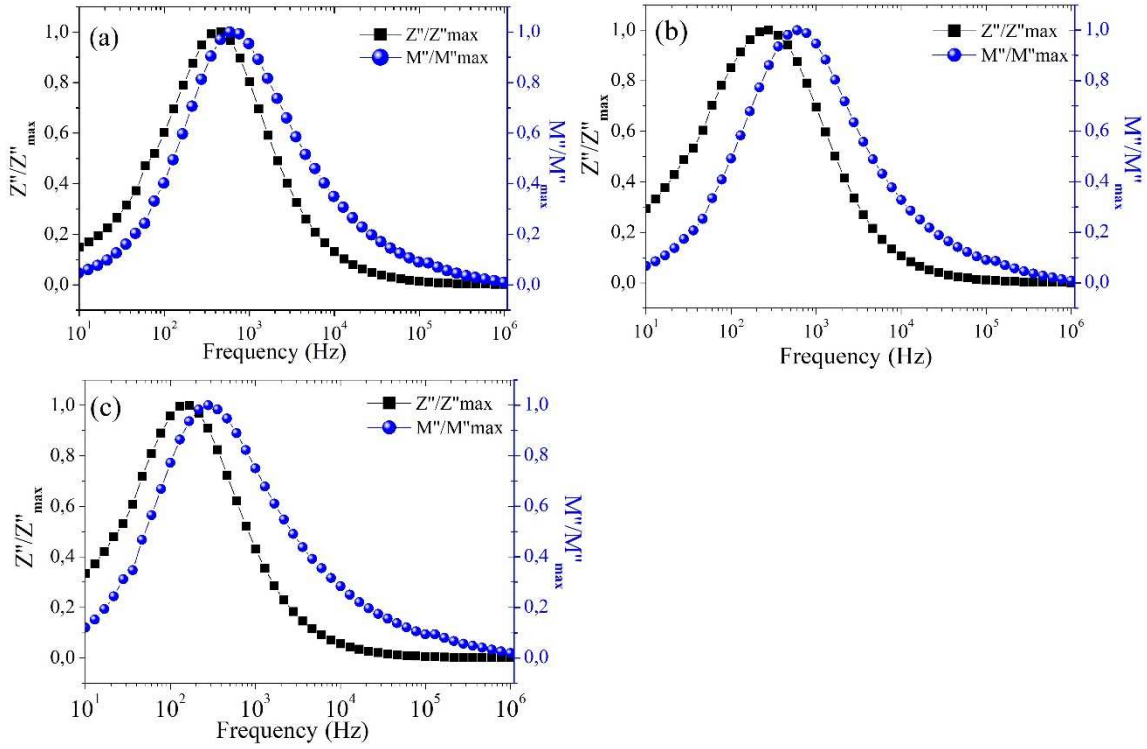
Fig. 18. Variation of Z''/Z''$_{MAX}$ and M''/M''$_{MAX}$ with frequency for Ba$_5$CaTi$_{2-x}$Zn$_x$Nb$_8$O$_{30}$ ceramics at 420°C; (a) x=0, (b) x=0.04, and (c) x=0.08.

4. Conclusion

Ba$_5$CaTi$_{2-x}$Zn$_x$Nb$_8$O$_{30}$ ceramics with (x=0, 0.04 and 0.08) were successfully synthesized by the solid state reaction route. Analysis of the XRD data by the Rietveld method showed a pure tetragonal tungsten bronze structure with the P4bm space group for all samples. The SEM images showed a homogeneous microstructure consisting of unequal sized grains, high densification, and low porosity. The average grain size was in the range of 1.3 to 1.6 μm. The dielectric constant decreases with increasing frequency, and dielectric losses increase with increasing temperature in the low frequency region because of the orientation of the dipole along the field which is facilitated by increasing temperature. The experimental data of the Nyquist plot has been successfully explained with the help of theoretical simulation, and it was found that grains and grain boundaries both contributed to the conduction process. The reduction in resistance with increasing temperature reveals the negative temperature coefficient of resistance (NTCR) behavior. The substitution of Ti^{4+} by Zn^{2+} increases the resistance value for grains and grain boundaries of the Ba$_5$CaTi$_{2-x}$Zn$_x$Nb$_8$O$_{30}$ ceramics. The values of Joncher's power law parameter suggest Correlated Barrier Hopping (CBH) mechanism for charge carriers. Two different activation energy regions were obtained by fitting of the Arrhenius formula at high temperature. They range from 0.340-0.387eV for grains and from 0.609-

0.748eV for grain boundaries, indicating that the single and doubly ionized oxygen vacancies are responsible for electrical conduction in $Ba_5CaTi_{2-x}Zn_xNb_8O_{30}$ ceramics. The modulus plot, i.e. M" vs. M', proved the contribution of grains and grain boundaries. The asymmetric nature of imaginary part of modulus indicated that relaxation processes observed in $Ba_5CaTi_{2-x}Zn_xNb_8O_{30}$ ceramics is non-Debye type in nature, with stretched parameter (β) at different temperatures between 0.4717 and 0.6087.

Acknowledgments

References

[1] J. Wu, D. Xiao, J. Zhu, Potassium–sodium niobate lead-free piezoelectric materials: past, present, and future of phase boundaries, Chemical reviews, 115 (2015) 2559-2595.

[2] Q. Li, M.-H. Zhang, Z.-X. Zhu, K. Wang, J.-S. Zhou, F.-Z. Yao, J.-F. Li, Poling engineering of $(K,Na)NbO_3$-based lead-free piezoceramics with orthorhombic–tetragonal coexisting phases, Journal of Materials Chemistry C, 5 (2017) 549-556.

[3] J.F. Li, K. Wang, F.Y. Zhu, L.Q. Cheng, F.Z. Yao, $(K,Na)NbO_3$-Based Lead-Free Piezoceramics: Fundamental Aspects, Processing Technologies, and Remaining Challenges, Journal of the American Ceramic Society, 96 (2013) 3677-3696.

[4] M.-H. Zhang, K. Wang, Y.-J. Du, G. Dai, W. Sun, G. Li, D. Hu, H.C. Thong, C. Zhao, X.-Q. Xi, High and temperature-insensitive piezoelectric strain in alkali niobate lead-free perovskite, Journal of the American Chemical Society, 139 (2017) 3889-3895.

[5] X.-D. Jian, B. Lu, D.-D. Li, Y.-B. Yao, T. Tao, B. Liang, J.-H. Guo, Y.-J. Zeng, J.-L. Chen, S.-G. Lu, Direct Measurement of Large Electrocaloric Effect in $Ba(Zr_xTi_{1-x})O_3$ Ceramics, ACS applied materials & interfaces, 10 (2018) 4801-4807.

[6] S. Hajra, S. Sahoo, R. Das, R. Choudhary, Structural, dielectric and impedance characteristics of $(Bi_{0.5}Na_{0.5})TiO_3$-$BaTiO_3$ electronic system, Journal of Alloys and Compounds, 750 (2018) 507-514.

[7] B. Wu, H. Wu, J. Wu, D. Xiao, J. Zhu, S.J. Pennycook, Giant piezoelectricity and high Curie temperature in nanostructured alkali niobate lead-free piezoceramics through phase coexistence, Journal of the American Chemical Society, 138 (2016) 15459-15464.

[8] A.D. Moriana, S. Zhang, Lead-free textured piezoceramics using tape casting: A review, Journal of Materiomics, 4 (2018) 277-303.

[9] J. Wu, Z. Fan, D. Xiao, J. Zhu, J. Wang, Multiferroic bismuth ferrite-based materials for multifunctional applications: ceramic bulks, thin films and nanostructures, Progress in Materials Science, 84 (2016) 335-402.

[10] T. Zheng, J. Wu, D. Xiao, J. Zhu, Recent development in lead-free perovskite piezoelectric bulk materials, Progress in materials science, 98 (2018) 552-624.

[11] M. Prades, H. Beltrán, N. Masó, E. Cordoncillo, A.R. West, Phase transition hysteresis and anomalous Curie–Weiss behavior of ferroelectric tetragonal tungsten bronzes $Ba_2RETi_2Nb_3O_{15}$: RE= Nd, Sm, Journal of Applied Physics, 104 (2008) 104118.

[12] I. Levin, M.C. Stennett, G.C. Miles, D.I. Woodward, A.R. West, I.M. Reaney, Coupling between octahedral tilting and ferroelectric order in tetragonal tungsten bronze-structured dielectrics, Applied physics letters, 89 (2006) 122908.

[13] B. Yang, S. Hao, P. Yang, L. Wei, Z. Yang, Relaxor behavior and energy storage density induced by B-sites substitutions in $(Ca_{0.28}Ba_{0.72})_{2.1}Na_{0.8}Nb_5O_{15}$ Tungsten bronze ceramics, Ceramics International, 44 (2018) 8832-8841.

[14] S. Jindal, A. Vasishth, S. Devi, G. Anand, A review on tungsten bronze ferroelectric ceramics as electrically tunable devices, Integrated Ferroelectrics, 186 (2018) 1-9.

[15] K. Shimizu, H. Kato, M. Kobayashi, M. Kakihana, Synthesis and photocatalytic properties of tetragonal tungsten bronze type oxynitrides, Applied Catalysis B: Environmental, 206 (2017) 444-448.

[16] K. Thummavichai, Y. Xia, Y. Zhu, Recent progress in chromogenic research of tungsten oxides towards energy-related applications, Progress in Materials Science, 88 (2017) 281-324.

[17] C. Huang, K. Li, X. Liu, X. Zhu, X. Chen, Effects of A1/A2-Sites Occupancy upon Ferroelectric Transition in $(Sr_xBa_{1-x})Nb_2O_6$ Tungsten Bronze Ceramics, Journal of the American Ceramic Society, 97 (2014) 507-512.

[18] Y. Yao, C. Mak, Effects of Ca-dopant on the pyroelectric, piezoelectric and dielectric properties of $(Sr_{0.6}Ba_{0.4})_4Na_2Nb_{10}O_{30}$ ceramics, Journal of alloys and compounds, 544 (2012) 87-93.

[19] K. Chandramouli, P. Viswarupachary, K. Ramam, Dielectric and pyroelectric properties of monovalent-lithium modified trivalent-samarium doped barium strontium sodium niobate tungsten bronze structured ceramics, Journal of Materials Science: Materials in Electronics, 20 (2009) 977-983.

[20] S. Abrahams, P. Jamieson, J. Bernstein, Ferroelectric tungsten bronze-type crystal structures. III. potassium lithium niobate $K_{(6-x-y)}Li_{(4+x)}Nb_{(10+y)}O_{30}$, The Journal of Chemical Physics, 54 (1971) 2355-2364.

[21] A. Bendahhou, P. Marchet, A. El-Houssaine, S. El Barkany, M. Abou-Salama, Relationship between structural and dielectric properties of Zn-substituted $Ba_5CaTi_{2-x}Zn_xNb_8O_{30}$ tetragonal tungsten bronze, CrystEngComm, 23 (2021) 163-173.

[22] J.B. Felder, W. Wong-Ng, R.A. Qabbani, R.S. Roth, B.H. Toby, J.Y.J.P. Chan, Structural investigation of the "tripled-tetragonal-tungsten-bronze" phases $Sr_2M_{10-x}O_{27-y}$ (M= Nb, Ta), Polyhedron, 170 (2019) 359-363.

[23] J.R. Macdonald, Impedance spectroscopy, Annals of biomedical engineering, 20 (1992) 289-305.

[24] N. Ortega, A. Kumar, R.S. Katiyar, C. Rinaldi, Investigation of temperature-dependent polarization, dielectric, and magnetization behavior of multiferroic layered nanostructure, Thin Solid Films, 519 (2010) 641-649.

[25] D. Cann, C.A. Randall, Electrode effects in positive temperature coefficient and negative temperature coefficient devices measured by complex-plane impedance analysis, Journal of applied physics, 80 (1996) 1628-1632.

[26] P. Ganguly, A. Jha, Investigations of structural, dielectric and electrical behaviour of calcium substituted $Ba_5NdTi_3Nb_7O_{30}$ ferroelectric ceramics, Integrated Ferroelectrics, 115 (2010) 149-156.

[27] R. Palai, R. Choudhary, H. Tewari, Structural and dielectric properties of $Ba_4R_2Ti_4Nb_6O_{30}$ (R= Y, Sm and Dy) ferroelectric ceramics, Journal of Physics and Chemistry of Solids, 62 (2001) 695-700.

[28] P.P. Rao, S. Ghosh, P. Koshy, Dielectric and ferroelectric properties of $Ba_3M_3Ti_5Nb_5O_{30}$ (M= Sm or Y) ceramics, Journal of Materials Science: Materials in Electronics, 12 (2001) 729-732.

[29] L. Fang, H. Zhang, J. Yang, F. Meng, R. Yuan, Structural and dielectric properties of ferroelectric $Sr_5RTi_3Nb_7O_{30}$ (R= Nd and Y) ceramics, Journal of materials science letters, 22 (2003) 1705-1707.

[30] S. Rani, N. Ahlawat, R. Punia, K.M. Sangwan, P. Khandelwal, Dielectric and impedance studies of La and Zn co-doped complex perovskite $CaCu_3Ti_4O_{12}$ ceramic, Ceramics International, 44 (2018) 23125-23136.

[31] Z. Guo, Q. Zhu, S. Wu, C. Hu, L. Liu, L. Fang, Effect of annealing atmosphere on the structure and dielectric properties of unfilled tungsten bronze ceramics $Ba_4PrFe_{0.5}Nb_{9.5}O_{30}$, Ceramics International, 44 (2018) 7700-7708.

[32] Z. Zhou, Y. Li, L. Yang, X. Dong, H. Yan, Effect of annealing on dielectric behavior and electrical conduction of W^{6+} doped Bi_3TiNbO_9 ceramics, Applied physics letters, 90 (2007) 212908.

[33] B.L. Deng, X.L. Zhu, X.Q. Liu, X.M. Chen, Effects of oxygen-deficiency on crystal structure, dielectric and ferroelectric properties in $Sr_5SmTi_{3+2x}Nb_{7-2x}O_{30-x}$ with tungsten bronze structure, RSC Advances, 7 (2017) 27370-27376.

[34] M. Prades, N. Masó, H. Beltran, E. Cordoncillo, A.R. West, Synthesis, Structural Characterization, and Electrical Properties of New Oxygen-Deficient Tetragonal Tungsten Bronzes $Ba_2NdTi_{2+x}Nb_{3-x}O_{15-x/2}$, Inorganic chemistry, 52 (2013) 1729-1736.

[35] P. Yang, B. Yang, S. Hao, L. Wei, Z. Yang, Variation of electrical properties with structural vacancies in ferroelectric niobates $(Sr_{0.53}Ba_{0.47})_{2.5-0.5x}Na_xNb_5O_{15}$ ceramics, Journal of Alloys and Compounds, 685 (2016) 175-185.

[36] S. Wu, C. Sun, X. Yang, C. Hu, L. Liu, L. Fang, Effect of strontium substitution on the structure and dielectric properties of unfilled tungsten bronze $Ba_{4-x}Sr_xSmFe_{0.5}Nb_{9.5}O_{30}$ ceramics, Ceramics International, 46 (2020) 9240-9248.

[37] A. Rotaru, F.D. Morrison, Microstructural and high-temperature impedance spectroscopy study of $Ba_6MNb_9O_{30}$ (M= Ga, Sc, In) relaxor dielectric ceramics with tetragonal tungsten bronze structure, Ceramics International, 42 (2016) 11810-11821.

[38] V. Petříček, M. Dušek, L. Palatinus, Crystallographic computing system JANA2006: general features, Zeitschrift für Kristallographie-Crystalline Materials, 229 (2014) 345-352.

[39] M. Arshad, H. Du, M.S. Javed, A. Maqsood, I. Ashraf, S. Hussain, W. Ma, H. Ran, Fabrication, structure, and frequency-dependent electrical and dielectric properties of Sr-doped $BaTiO_3$ ceramics, Ceramics International, 46 (2020) 2238-2246.

[40] J. Joshi, D. Kanchan, M. Joshi, H. Jethva, K. Parikh, Dielectric relaxation, complex impedance and modulus spectroscopic studies of mix phase rod like cobalt sulfide nanoparticles, Materials Research Bulletin, 93 (2017) 63-73.

[41] K.S. Udupa, P.M. Rao, S. Aithal, A. Bhat, D. Avasthi, Effect of heavy-ion irradiation on dielectric constant and electrical conductivity of doped and undoped nonlinear substance, Bulletin of materials science, 20 (1997) 1069-1077.

[42] B. Arya, R. Choudhary, Structural, dielectric and electrical properties of $BaSnO_3$ and $BaSeO_3$ modified $Bi_{0.5}Na_{0.5}TiO_3$ ceramics, Ceramics International, 46 (2020) 4222-4234.

[43] D.C. Sinclair, A.R. West, Impedance and modulus spectroscopy of semiconducting $BaTiO_3$ showing positive temperature coefficient of resistance, Journal of Applied Physics, 66 (1989) 3850-3856.

[44] H. Ali, S. Karim, M. Rafiq, K. Maaz, A. ur Rahman, A. Nisar, M. Ahmad, Electrical conduction mechanism in ZnS nanoparticles, Journal of alloys and compounds, 612 (2014) 64-68.

[45] J.R. Macdonald, E. Barsoukov, Impedance spectroscopy: theory, experiment, and applications, History, 1 (2005) 1-13.

[46] A. Yadav, S.P. Mantry, M. Fahad, P. Sarun, Temperature dependent dielectric relaxation and ac–conductivity of alkali niobate ceramics studied by impedance spectroscopy, Physica B: Condensed Matter, 537 (2018) 290-295.

[47] A. Franco Jr, P. Banerjee, P. Romanholo, Effect of composition induced transition in the optical band-gap, dielectric and magnetic properties of Gd doped $Na_{0.5}Bi_{0.5}TiO_3$ complex perovskite, Journal of Alloys and Compounds, 764 (2018) 122-127.

[48] J.R. Macdonald, Note on the parameterization of the constant-phase admittance element, Solid State Ionics, 13 (1984) 147-149.

[49] P. Gupta, R. Padhee, P. Mahapatra, R. Choudhary, Structural and electrical characteristics of Bi_2YTiVO_9 ceramic, Materials Research Express, 5 (2018) 045905.

[50] P. Gupta, P. Mahapatra, R. Choudhary, Investigation on structural and electrical properties of Co and W modified $BaTiO_3$, Ceramics International, 45 (2019) 22862-22871.

[51] P. Gupta, R. Padhee, P. Mahapatra, R. Choudhary, S. Das, Structural and electrical properties of Bi_3TiVO_9 ferroelectric ceramics, Journal of Alloys and Compounds, 731 (2018) 1171-1180.

[52] P. Gupta, P. Mahapatra, R. Choudhary, Investigations on structural and electrical characteristics of Fe and W modified $BaTiO_3$ ceramic, Physica B: condensed matter, 572 (2019) 203-213.

[53] M. Chaari, R.B. Belgacem, A. Matoussi, Impedance analysis, dielectric relaxation and modulus behaviour of $ZnO-Sn_2O_3$ ceramics, Journal of Alloys and Compounds, 726 (2017) 49-56.

[54] A.K. Jonscher, The 'universal'dielectric response, nature, 267 (1977) 673-679.

[55] D.K. Pradhan, B. Behera, P.R. Das, Studies of dielectric and electrical properties of a new type of complex tungsten bronze electroceramics, Journal of Materials Science: Materials in Electronics, 23 (2012) 779-785.

[56] K. Funke, Jump relaxation in solid ionic conductors, Solid State Ionics, 28 (1988) 100-107.

[57] S.S. Shah, K. Hayat, S. Ali, K. Rasool, Y. Iqbal, Conduction mechanisms in lanthanum manganite nanofibers, Materials Science in Semiconductor Processing, 90 (2019) 65-71.

[58] S. Elliott, Ac conduction in amorphous chalcogenide and pnictide semiconductors, Advances in physics, 36 (1987) 135-217.

[59] R. Muhammad, A. Khesro, M. Uzair, Dielectric properties and complex impedance analysis of BT–BMT–BS ceramics, Journal of Electronic Materials, 45 (2016) 4083-4088.

[60] J. Scott, M. Dawber, Oxygen-vacancy ordering as a fatigue mechanism in perovskite ferroelectrics, Applied Physics Letters, 76 (2000) 3801-3803.

[61] G. Singh, V. Tiwari, P. Gupta, Role of oxygen vacancies on relaxation and conduction behavior of $KNbO_3$ ceramic, Journal of Applied Physics, 107 (2010) 064103.

[62] J. Miao, X. Xu, Y. Jiang, L. Cao, B. Zhao, Ionized-oxygen vacancies related dielectric relaxation in heteroepitaxial $K_{0.5}Na_{0.5}NbO_3/La_{0.67}Sr_{0.33}MnO_3$ structure at elevated temperature, Applied Physics Letters, 95 (2009) 132905.

[63] A. Peláiz-Barranco, J. Guerra, Dielectric relaxation related to single-ionized oxygen vacancies in $(Pb_{1-x}La_x)(Zr_{0.90}Ti_{0.10})_{1-x/4}O_3$ ceramics, Materials Research Bulletin, 45 (2010) 1311-1313.

[64] Q. Li, H. Wang, H. Fan, M. Xu, B. Peng, C. Long, X. Liu, Dielectric properties and electrical conduction of La_2O_3-doped $(Bi_{0.5}Na_{0.5})_{0.94}Ba_{0.06}TiO_3$ ceramics, Applied Physics A, 114 (2014) 551-558.

[65] L. Liu, Y. Huang, Y. Li, M. Wu, L. Fang, C. Hu, Y. Wang, Oxygen-vacancy-related high-temperature dielectric relaxation and electrical conduction in $0.95K_{0.5}Na_{0.5}NbO_3–0.05BaZrO_3$ ceramic, Physica B: Condensed Matter, 407 (2012) 136-139.

[66] A. Bendahhou, K. Chourti, R. El Bouayadi, S. El Barkany, M. Abou-Salama, Structural, dielectric and impedance spectroscopy analysis of $Ba_5CaTi_{1.94}Zn_{0.06}Nb_8O_{30}$ ferroelectric ceramic, RSC Advances, 10 (2020) 28007-28018.

[67] U. Balachandran, B. Odekirk, N. Eror, Defect structure of acceptor-doped calcium titanate at elevated temperatures, Journal of Materials Science, 17 (1982) 1656-1662.

[68] S. Hosseini, K. Ranjbar, R. Dehmolaei, A. Amirani, Fabrication of Al5083 surface composites reinforced by CNTs and cerium oxide nano particles via friction stir processing, Journal of Alloys and Compounds, 622 (2015) 725-733.

[69] T. Badapanda, V. Senthil, S. Rout, L. Cavalcante, A.Z. Simões, T. Sinha, S. Panigrahi, M. De Jesus, E. Longo, J.A. Varela, Rietveld refinement, microstructure, conductivity and impedance properties of $Ba[Zr_{0.25}Ti_{0.75}]O_3$ ceramic, Current Applied Physics, 11 (2011) 1282-1293.

[70] K.S. Cole, R.H. Cole, Dispersion and absorption in dielectrics I. Alternating current characteristics, The Journal of chemical physics, 9 (1941) 341-351.

[71] Y. Wong, J. Hassan, M. Hashim, Dielectric properties, impedance analysis and modulus behavior of $CaTiO_3$ ceramic prepared by solid state reaction, Journal of alloys and compounds, 571 (2013) 138-144.

[72] K. Padmasree, D. Kanchan, A. Kulkarni, Impedance and Modulus studies of the solid electrolyte system $20CdI_2–80[xAg_2O–y(0.7V_2O_5–0.3B_2O_3)]$, where $1 \leq x/y \leq 3$, Solid State Ionics, 177 (2006) 475-482.

[73] B. Chowdari, R. Gopalakrishnan, AC conductivity analysis of glassy silver iodomolybdate system, Solid State Ionics, 23 (1987) 225-233.

[74] S. Brahma, R. Choudhary, A.K. Thakur, AC impedance analysis of $LaLiMo_2O_8$ electroceramics, Physica B: Condensed Matter, 355 (2005) 188-201.

[75] S.K. Barik, R. Choudhary, A. Singh, Ac impedance spectroscopy and conductivity studies of $Ba_{0.8}Sr_{0.2}TiO_3$ ceramics, Adv. Mat. Lett, 2 (2011) 419-424.

[76] R. Bergman, General susceptibility functions for relaxations in disordered systems, Journal of Applied Physics, 88 (2000) 1356-1365.

[77] J.C. Fernandes, R.A.S. Nascimento, M. Mulato, Effects of Measurements Conditions on an Extended-Gate FET used as pH sensor, Materials Research, 19 (2016) 267-272.